JETP Letters, Vol. 76, No. 4, 2002, pp. 195–200. From Pis'ma v Zhurnal Éksperimental'noĭ i Teoreticheskoĭ Fiziki, Vol. 76, No. 4, 2002, pp. 231–235.


# Saturation of Nuclear Partons: Fermi Statistics or Nuclear Opacity?¶

**N. N. Nikolaev[1, 2], W. Schäfer[3], B. G. Zakharov[2], and V. R. Zoller[4]**

[1] *Institut f. Kernphysik, Forschungszentrum Jülich, Jüilich, D-52425 Germany*
*e-mail: N.Nikolaev@fz-juelich.de*
[2] *Landau Institute for Theoretical Physics, RAS, Chernogolovka, 142432 Russia*
[3] *NORDITA, DK-2100 Copenhagen Ø, Denmark*
[4] *Institute for Theoretical and Experimental Physics, Moscow, 117218 Russia*

Received July 10, 2002

We derive the two-plateau momentum distribution of final state (FS) quarks produced in deep inelastic scattering (DIS) off nuclei in the saturation regime. The diffractive plateau, which dominates for small **p**, measures precisely the momentum distribution of quarks in the beam photon; the role of the nucleus is simply to provide an opacity. The plateau for truly inelastic DIS exhibits a substantial nuclear broadening of the FS momentum distribution. We discuss the relationship between the FS quark densities and the properly defined initial state (IS) nuclear quark densities. The Weizsäcker–Williams glue of a nucleus exhibits a substantial nuclear dilution, still soft IS nuclear sea saturates because of the anti-collinear splitting of gluons into sea quarks. © *2002 MAIK "Nauka/Interperiodica".*

PACS numbers: 24.85.+p

The interpretation of nuclear opacity in terms of the fusion and saturation of nuclear partons was introduced in 1975 [1] long before the QCD parton model: the Lorentz contraction of relativistic nuclei entails a spatial overlap of partons with $x \lesssim x_A \approx 1/R_A m_N$ from different nucleons, and the fusion of overlapping partons results in the saturation of parton densities per unit area in the impact parameter space. The pQCD link between nuclear opacity and saturation was considered by Mueller [2], and the pQCD discussion of fusion of nuclear gluons was revived by McLerran *et al.* [3].

The common wisdom is that in deep inelastic scattering (DIS), final-state (FS) interaction effects can be neglected and the observed momentum distribution of struck partons in the FS coincides with the initial state (IS) density of partons in the probed hadron. Based on the consistent treatment of intranuclear distortions, we derive the two-plateau spectrum of FS quarks. We find a substantial nuclear broadening of inclusive FS spectra and demonstrate that despite this broadening, the FS sea parton density exactly equals the IS sea parton density calculated in terms of the Weizsäcker–Williams (WW) glue of the nucleus as defined according to [4]. We pay special attention to an important point that the diffractive DIS, in which the target nucleus does not break, is retained in the ground state, and is responsible for precisely 50 percent of the total DIS events [5]. We point out that the saturated diffractive plateau measures precisely the momentum distribution of (anti-)quarks in the $q\bar{q}$ Fock state of the photon. In contrast to DIS off nuclei, the fraction of DIS off free nucleons which is diffractive is negligibly small [6], $\eta_D \lesssim$ 6–10%, and there is little room for genuine saturation effects even at HERA. We show how the anti-collinear splitting of WW gluons into sea quarks gives rise to nuclear saturation of the sea despite a substantial nuclear dilution of the WW glue.

We base our analysis on the color dipole formulation of DIS [5, 7–10] and illustrate our ideas on an example of DIS at $x \sim x_A \ll 1$ which is dominated by interactions of $q\bar{q}$ states of the photon. The total cross section for interaction of the color dipole **r** with the target nucleon equals

$$\sigma(r) = \alpha_S(r)\sigma_0 \int d^2\boldsymbol{\kappa} f(\boldsymbol{\kappa})[1 - \exp(i\boldsymbol{\kappa}\mathbf{r})], \qquad (1)$$

where $f(\boldsymbol{\kappa})$ is related to the unintegrated glue of the target nucleon by

$$f(\boldsymbol{\kappa}) = \frac{4\pi}{N_c\sigma_0}\frac{1}{\kappa^4}\frac{\partial G}{\partial \log \kappa^2}, \quad \int d^2\boldsymbol{\kappa} f(\boldsymbol{\kappa}) = 1. \qquad (2)$$

For DIS off a free nucleon target (see Figs. 1a–1d) the momentum spectrum of the FS quark prior the hadronization,

$$\frac{d\sigma_N}{d^2\mathbf{p}\,dz} = \frac{\sigma_0}{2}\frac{\alpha_S(\mathbf{p}^2)}{(2\pi)^2}\int d^2\boldsymbol{\kappa} f(\boldsymbol{\kappa})|\langle\gamma^*|\mathbf{p}\rangle - \langle\gamma^*|\mathbf{p}-\boldsymbol{\kappa}\rangle|^2, \qquad (3)$$

¶This article was submitted by the authors in English.

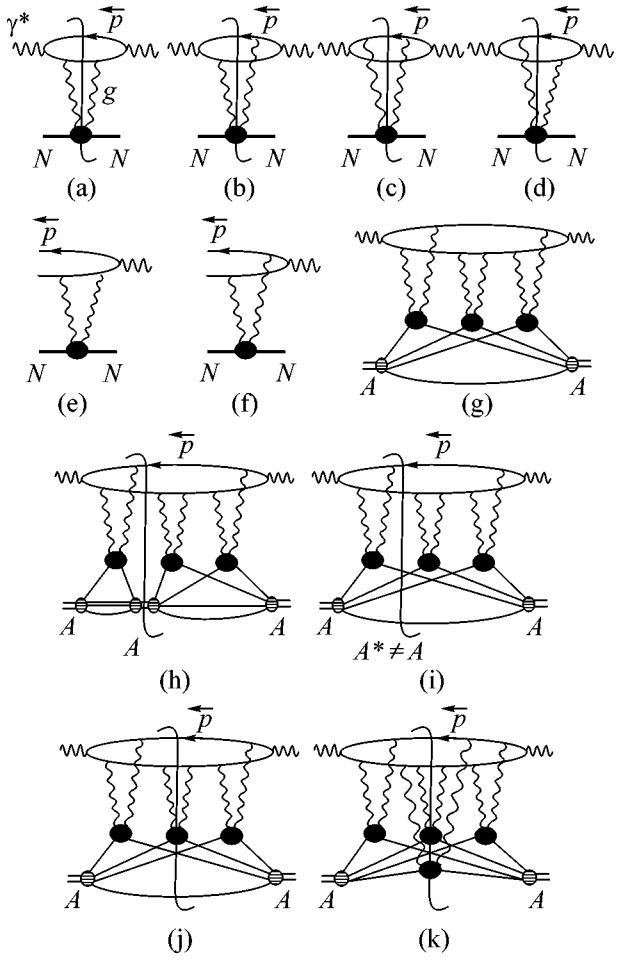


**Fig. 1.** The pQCD diagrams for (a)–(d) inclusive and (e), (f) diffractive DIS off protons and (g)–(k) nuclei. Diagrams (a–d) show the unitarity cuts with color excitation of the target nucleon, (g) is a generic multiple scattering diagram for Compton scattering off nucleus, (h) is the unitarity cut for a coherent diffractive DIS, (i) is the unitarity cut for quasielastic diffractive DIS with excitation of the nucleus $A^*$, and (j) and (k) are the unitarity cuts for truly inelastic DIS with single and multiple color excitation of nucleons of the nucleus.

where $\mathbf{p}$ is the transverse momentum and $z$ is the Feynman variable, coincides upon integration over $z$, with the conventional IS unintegrated $\mathbf{p}$ distribution of partons in the target. Notice that the target nucleon is color-excited and that there is no rapidity gap in the FS.

In DIS off nuclei, one must distinguish the three principal processes with distinct unitarity cuts of the forward Compton amplitude (Fig. 1g): the coherent diffraction dissociation (*D*) of the photon (Fig. 1h), quasielastic diffraction dissociation (*qel*) followed by excitation and breakup of the target nucleus (Fig. 1i) (in both of these processes, there is no color flow between the photon debris and the nucleus), and the truly inelastic (*in*) DIS with color excitation of nucleons of the target nucleus (Figs. 1j, 1k). Useful guidance for the isolation of different processes comes from the coupled-channel formalism presented in [11].

We work in the conventional approximation of two *t*-channel gluons in DIS off free nucleons, Figs. 1a–1d, i.e., neglecting the effect of diffractive DIS (Figs. 1e, 1f) on the total cross section on free nucleons, $\eta_D \ll 1$. Then, the *S*-matrix of the quark–nucleon scattering must be computed to the second order in the QCD eikonal $\delta(\mathbf{b})$, and the *S*-matrix for the color dipole-nucleon scattering takes the form

$$S(\mathbf{b}_+, \mathbf{b}_-) = 1 + 2i[\Delta(\mathbf{b}_+) - \Delta(\mathbf{b}_-)] - 2\langle[\delta(\mathbf{b}_+) - \delta(\mathbf{b}_-)]^2\rangle_0. \quad (4)$$

Here, $\langle\ldots\rangle_0$ indicates that we must take only the color singlet component of the two-gluon exchange and we have introduced special notation $\Delta(\mathbf{b}) = \delta(\mathbf{b})$ for the color-exchange component of the *S*-matrix. The color dipole cross section equals $\sigma(\mathbf{r}) = 2\int d^2\mathbf{b}\{1 - \langle S(\mathbf{b} + \mathbf{r}, \mathbf{b})\rangle_0\}$, which relates the QCD eikonal to the gluon structure function of the nucleon,

$$\int d^2\mathbf{b}\,\langle\delta(\mathbf{b} + \mathbf{r})\delta(\mathbf{b})\rangle_0 = \frac{1}{8}\alpha_S(\mathbf{r})\sigma_0\int d^2\boldsymbol{\kappa} f(\boldsymbol{\kappa})\exp[i\boldsymbol{\kappa}\mathbf{r}]. \quad (5)$$

If in the nuclear *S*-matrix $S_A(\{\Delta\}, \{\delta\}; \mathbf{b}_+, \mathbf{b}_-) = \prod_{j=1}^{A} S(\mathbf{b}_+ - \mathbf{b}_j, \mathbf{b}_- - \mathbf{b}_j)$ one puts $\Delta(\mathbf{b}_\pm - \mathbf{b}_j) \equiv 0$, then it would describe pure diffraction without color excitations in a nucleus. Then, with standard reference to closure [11], the momentum spectrum of observed FS quarks for truly inelastic DIS with color excitations in the nucleus can readily be isolated:

$$\frac{d\sigma_{\rm in}}{dz d^2\mathbf{p}_+ d^2\mathbf{p}_-} = \frac{1}{(2\pi)^4}\int d^2\mathbf{b}'_+ d^2\mathbf{b}'_- d^2\mathbf{b}_+ d^2\mathbf{b}_- \times \exp[-i\mathbf{p}_+(\mathbf{b}_+ - \mathbf{b}'_+) - i\mathbf{p}_-(\mathbf{b}_- - \mathbf{b}'_-)] \times \Psi^*(\mathbf{b}'_+ - \mathbf{b}'_-)\Psi(\mathbf{b}_+ - \mathbf{b}_-) \quad (6)$$
$$\times\{\langle A|S_A^*(\{\Delta\}, \{\delta\}; \mathbf{b}'_+, \mathbf{b}'_-)S_A(\{\Delta\}, \{\delta\}; \mathbf{b}_+, \mathbf{b}_-)|A\rangle - \langle A|S_A^*(0, \{\delta\}; \mathbf{b}'_+, \mathbf{b}'_-)S_A(0, \{\delta\}; \mathbf{b}_+, \mathbf{b}_-)|A\rangle\}.$$

Here, $\Psi$ is the $q\bar{q}$-Fock state wave function of the virtual photon and we have suppressed its dependence on $z$. The FS spectra in the coherent and quasielastic diffraction are obtained by substituting

$$\{\ldots\}_D = \langle A|1 - S_A^*(0, \{\delta\}; \mathbf{b}'_+, \mathbf{b}'_-)|A\rangle \times \langle A|1 - S_A(0, \{\delta\}; \mathbf{b}_+, \mathbf{b}_-)|A\rangle, \quad (7)$$

$$\{\dots\}_{\rm qel}$$

$$= \{\langle A|S_A^*(0,\{\delta\};\mathbf{b}'_+,\mathbf{b}'_-)S_A(0,\{\delta\};\mathbf{b}_+,\mathbf{b}_-)|A\rangle \quad (8)$$

$$-\langle A|S_A^*(0,\{\delta\};\mathbf{b}'_+,\mathbf{b}'_-)|A\rangle\langle A|S_A(0,\{\delta\};\mathbf{b}_+,\mathbf{b}_-)|A\rangle\}$$

for the expression in the curly braces.

The size of color dipoles can be neglected compared to the radius of heavy nuclei. In the standard approximation of a dilute gas nucleus, only the color-singlet terms $\propto\langle\Delta(\mathbf{b}_1)\Delta(\mathbf{b}_2)\rangle_0$ would appear in (6), and we find

$$\langle A|S_A^*(\{\Delta\},\{\delta\};\mathbf{b}'_+,\mathbf{b}'_-)S_A(\{\Delta\},\{\delta\};\mathbf{b}_+,\mathbf{b}_-)|A\rangle$$

$$= \exp\left\{-\frac{1}{2}T(\mathbf{b})[\Sigma(\mathbf{b}'_+-\mathbf{b}_+)+\Sigma(\mathbf{b}'_--\mathbf{b}_-)\right.$$
$$-\Sigma(\mathbf{b}'_+-\mathbf{b}_-)-\Sigma(\mathbf{b}_+-\mathbf{b}'_-) \quad (9)$$
$$\left.+\sigma(\mathbf{b}'_+-\mathbf{b}'_-)+\sigma(\mathbf{b}_+-\mathbf{b}_-)]\right\},$$

where $T(\mathbf{b}) = \int dz\, n_A(z,\mathbf{b})$ is the optical thickness of a nucleus at an impact parameter $\mathbf{b}\approx\mathbf{b}_\pm, \mathbf{b}'_\pm$. Here, $\Sigma(\mathbf{r}) = \sigma(\mathbf{r})$; we use the capital letter to indicate that it originates from the color excitation processes, whereas the last two terms in the exponent of (9) describe intranuclear attenuation of the $q\bar{q}$ pair due to color-singlet exchanges. The diffractive $S$-matrix elements entering (7), (8) are readily obtained from (9). For a heavy nucleus, the quasielastic diffraction is a surface phenomenon and can be neglected for all the practical purposes, see [5]; it vanishes to the considered leading order (4). If we are interested only in the single particle spectrum and integrate over $\mathbf{p}_-$, then $\mathbf{b}'_- = \mathbf{b}_-$, and the diffractive attenuation terms in the exponent of (9) would exactly cancel the two terms from multiple color excitation processes in the last line of (9), and

$$\frac{d\sigma_{\rm in}}{d^2\mathbf{p}dz} = \frac{1}{(2\pi)^2}$$
$$\times\int d^2\mathbf{b}\int d^2\mathbf{r}'d^2\mathbf{r}\exp[i\mathbf{p}(\mathbf{r}'-\mathbf{r})]\Psi^*(\mathbf{r}')\Psi(\mathbf{r})$$
$$\left\{\exp\left[-\frac{1}{2}\sigma(\mathbf{r}-\mathbf{r}')T(\mathbf{b})\right]\right. \quad (10)$$
$$\left.-\exp\left[-\frac{1}{2}[\sigma(\mathbf{r})+\sigma(\mathbf{r}')]T(\mathbf{b})\right]\right\}.$$

Evidently, the dependence of nuclear attenuation factors on $\mathbf{r}$, $\mathbf{r}'$ shall distort strongly the observed momentum distribution of quarks.

In the further interpretation of these results in terms of the parton model, we resort to the representation [4] (NSS)

$$\Gamma_A(\mathbf{b},\mathbf{r}) = 1-\exp\left[-\frac{1}{2}\sigma(r)T(\mathbf{b})\right]$$
$$= \int d^2\boldsymbol{\kappa}\phi_{WW}(\boldsymbol{\kappa})[1-\exp(i\boldsymbol{\kappa}\mathbf{r})]. \quad (11)$$

Driven by a close analogy to (1), (2) in terms of $f(\boldsymbol{\kappa})$, we interpret

$$\phi_{WW}(\boldsymbol{\kappa}) = \sum_{j=1}^{\infty}\nu_A^j(\mathbf{b})\cdot\frac{1}{j!}f^{(j)}(\boldsymbol{\kappa})\exp[-\nu_A(\mathbf{b})] \quad (12)$$

as the WW unintegrated glue of a nucleus per unit area in the impact parameter plane. It is normalized as

$$\int d^2\boldsymbol{\kappa}\phi_{WW}(\boldsymbol{\kappa}) = 1-\exp[-\nu_A(\mathbf{b})]. \quad (13)$$

Here,

$$\nu_A(\mathbf{b}) = \frac{1}{2}\alpha_S(r)\sigma_0 T(\mathbf{b})$$

defines the nuclear opacity, and the $j$-fold convolutions

$$f^{(j)}(\boldsymbol{\kappa}) = \int\prod_{i=1}^{j}d^2\boldsymbol{\kappa}_i f(\boldsymbol{\kappa}_i)\delta\left(\boldsymbol{\kappa}-\sum_{i=1}^{j}\boldsymbol{\kappa}_i\right) \quad (14)$$

describe the contribution to the diffractive amplitudes from $j$ split pomerons [4].

A discussion of the nuclear antishadowing property of the hard WW glue is found in [4]. A somewhat involved analysis of the properties of the convolutions (14) in the soft region shows that they develop a plateau-like behavior, with the width of the plateau expanding $\propto j$. The gross features of the WW nuclear glue in the soft region are well reproduced by

$$\phi_{WW}(\boldsymbol{\kappa})\approx\frac{1}{\pi}\frac{Q_A^2}{(\boldsymbol{\kappa}^2+Q_A^2)^2}, \quad (15)$$

where the saturation scale $Q_A^2 = \nu_A(\mathbf{b})Q_0^2 \propto A^{1/3}$. The soft parameters $Q_0^2$ and $\sigma_0$ are related to the integrated glue of the proton in the soft region,

$$Q_0^2\sigma_0 \sim \frac{2\pi^2}{N_c}G_{\rm soft}, \quad G_{\rm soft}\sim 1.$$

Notice the nuclear dilution of soft WW glue, $\phi_{WW}(\boldsymbol{\kappa})\propto 1/Q_A^2 \propto A^{-1/3}$.

On the one hand, making use of the NSS representation, the total nuclear photoabsorption cross section can be cast in the form

$$\sigma_A = \int d^2\mathbf{b}\int dz\int\frac{d^2\mathbf{p}}{(2\pi)^2} \times\int d^2\boldsymbol{\kappa}\phi_{WW}(\boldsymbol{\kappa})|\langle\gamma^*|\mathbf{p}\rangle-\langle\gamma^*|\mathbf{p}-\boldsymbol{\kappa}\rangle|^2, \quad (16)$$

which has a profound resemblance to (3), and one is tempted to take the differential form of (16) as a definition of the IS sea quark density in a nucleus:

$$\frac{d\bar{q}_{IS}}{d^2\mathbf{b}d^2\mathbf{p}} = \frac{1}{2}\frac{Q^2}{4\pi^2\alpha_{em}}\frac{d\sigma_A}{d^2\mathbf{b}d^2\mathbf{p}}. \quad (17)$$

In terms of the WW nuclear glue, all intranuclear multiple-scattering diagrams of Fig. 1g sum up to precisely the same four diagrams Figs. 1a–1d as in DIS off free nucleons. Furthermore, one can argue that the small-$x$ evolution of the so-defined IS nuclear sea is similar to that for a free nucleon sea. Although $\mathbf{p}$ emerges here just as a formal Fourier parameter, we shall demonstrate that it can be identified with the momentum of the observed final state antiquark.

On the other hand, making use of the NSS representation, after some algebra, one finds

$$\exp\left[-\frac{1}{2}\sigma(\mathbf{r}-\mathbf{r}')T(\mathbf{b})\right]-\exp\left[-\frac{1}{2}[\sigma(\mathbf{r})+\sigma(\mathbf{r}')]T(\mathbf{b})\right]$$
$$=\int d^2\boldsymbol{\kappa}\phi_{WW}(\boldsymbol{\kappa})\{(\exp[i\boldsymbol{\kappa}(\mathbf{r}-\mathbf{r}')]-1)$$
$$+(1-\exp[i\boldsymbol{\kappa}\mathbf{r}])+(1-\exp[i\boldsymbol{\kappa}\mathbf{r}'])\} \quad (18)$$
$$-\int d^2\boldsymbol{\kappa}\phi_{WW}(\boldsymbol{\kappa})(1-\exp[i\boldsymbol{\kappa}\mathbf{r}])$$
$$\times\int d^2\boldsymbol{\kappa}'\phi_{WW}(\boldsymbol{\kappa}')(1-\exp[i\boldsymbol{\kappa}'\mathbf{r}']),$$

$$\frac{d\sigma_{\rm in}}{d^2\mathbf{b}d^2\mathbf{p}dz} = \frac{1}{(2\pi)^2}$$
$$\times\left\{\int d^2\boldsymbol{\kappa}\phi_{WW}(\boldsymbol{\kappa})|\langle\gamma^*|\mathbf{p}\rangle-\langle\gamma^*|\mathbf{p}-\boldsymbol{\kappa}\rangle|^2\right. \quad (19)$$
$$\left.-\left|\int d^2\boldsymbol{\kappa}\phi_{WW}(\boldsymbol{\kappa})(\langle\gamma^*|\mathbf{p}\rangle-\langle\gamma^*|\mathbf{p}-\boldsymbol{\kappa}\rangle)\right|^2\right\},$$

$$\frac{d\sigma_D}{d^2\mathbf{b}d^2\mathbf{p}dz} = \frac{1}{(2\pi)^2}\left|\int d^2\boldsymbol{\kappa}\phi_{WW}(\boldsymbol{\kappa})(\langle\gamma^*|\mathbf{p}\rangle-\langle\gamma^*|\mathbf{p}-\boldsymbol{\kappa}\rangle)\right|^2. \quad (20)$$

As far as diffraction is concerned, the analogy between (20) and its counterpart for free nucleons [4, 8, 12] and nuclear WW glue $\phi_{WW}(\boldsymbol{\kappa})$ and $f(\boldsymbol{\kappa})$ thereof, is complete. Putting the inelastic and diffractive components of the FS quark spectrum together, we evidently find the FS parton density which exactly coincides with the IS parton density (17) such that $\mathbf{p}$ is indeed the transverse momentum of the FS sea quark. The interpretation of this finding is not trivial, though.

Consider first the domain of $\mathbf{p}^2 \lesssim Q^2 \lesssim Q_A^2$ that the nucleus is opaque for all color dipoles in the photon. Hereafter, we assume that the saturation scale $Q_A^2$ is so large that $\mathbf{p}^2$, $Q^2$ are in the pQCD domain and neglect the quark masses. In this regime the nuclear counterparts of the crossing diagrams of Figs. 1b, 1d, 1f can be neglected. Then, in the classification of [4], diffraction will be dominated by the contribution from the Landau-Pomeranchuk diagram of Fig. 1e with the result

$$\left.\frac{d\bar{q}_{FS}}{d^2\mathbf{b}d^2\mathbf{p}}\right|_D = \frac{1}{2}\frac{Q^2}{4\pi^2\alpha_{em}}\frac{d\sigma_D}{d^2\mathbf{b}d^2\mathbf{p}}$$
$$\approx\frac{1}{2}\frac{Q^2}{4\pi^2\alpha_{em}}\int dz\left|\int d^2\boldsymbol{\kappa}\phi_{WW}(\boldsymbol{\kappa})\right|^2|\langle\gamma^*|\mathbf{p}\rangle|^2\approx\frac{N_c}{4\pi^4}. \quad (21)$$

Up to now, we specified neither the wave function of the photon nor the spin nor the color representation of charged partons; only the last result in (17) makes explicit use of the conventional spin-$\frac{1}{2}$ partons. We also used the normalization (13). Remarkably, diffractive DIS measures the momentum distribution of quarks and antiquarks in the $q\bar{q}$ Fock state of the photon. We emphasize that this result, typical of the Landau–Pomeranchuk mechanism, is a completely generic one and would hold for any beam particle such that its coupling to colored partons is weak. In contrast to diffraction off free nucleons [8, 12, 13], diffraction off opaque nuclei is dominated by the anti-collinear splitting of hard gluons into soft sea quarks, $\boldsymbol{\kappa}^2 \gg \mathbf{p}^2$. Precisely for this reason one finds the saturated FS quark density, because the nuclear dilution of the WW glue is compensated for by the expanding plateau. The result (21) has no counterpart in DIS off free nucleons because diffractive DIS off free nucleons is negigibly small even at HERA, $\eta_D \lesssim 6$–$10\%$.

The related analysis of the FS quark density for truly inelastic DIS in the same domain of $\mathbf{p}^2 \lesssim Q^2 \lesssim Q_A^2$ gives

$$\left.\frac{d\bar{q}_{FS}}{d^2\mathbf{b}d^2\mathbf{p}}\right|_{\rm in} = \frac{1}{2}\frac{Q^2}{4\pi^2\alpha_{em}}$$

$$\times \int dz \int d^2\boldsymbol{\kappa}\phi_{WW}(\boldsymbol{\kappa})|\langle\gamma^*|\mathbf{p}-\boldsymbol{\kappa}\rangle|^2$$
$$= \frac{Q^2}{8\pi^2\alpha_{em}}\phi_{WW}(0)\int^{Q^2} d^2\boldsymbol{\kappa}\int dz|\langle\gamma^*|\boldsymbol{\kappa}\rangle|^2 \quad (22)$$
$$= \frac{N_c}{4\pi^4}\frac{Q^2}{Q_A^2}\theta(Q_A^2-\mathbf{p}^2).$$

It describes the final states with color excitation of a nucleus. However, as a function of the photon wave function and the nuclear WW gluon distribution, it is completely different from Eq. (3) for free nucleons. The θ-function simply indicates that the plateau for inelastic DIS extends up to $\mathbf{p}^2 \lesssim Q_A^2$. For $Q^2 \ll Q_A^2$, the inelastic plateau contributes little to the transverse momentum distribution of soft quarks, $\mathbf{p}^2 \lesssim Q^2$, but the inelastic plateau extends far beyond $Q^2$, and its integral contribution to the spectrum of FS quarks is exactly equal to that from diffractive DIS. Such a two-plateau structure of the FS quark spectrum is a new finding and has not been considered before.

Now notice that in the opacity regime, the diffractive FS parton density coincides with the contribution $\propto|\langle\gamma^*|\mathbf{p}\rangle|^2$ to the IS sea parton density from the spectator diagram 1a, whereas the FS parton density for truly inelastic DIS coincides with the contribution to IS sea partons from the diagram of Fig. 1c. The contribution from the crossing diagrams 1b, 1d is negigibly small.

Our results (21) and (22), especially nuclear broadening and unusually strong $Q^2$ dependence of the FS/IS parton density from truly inelastic DIS, clearly demonstrate a distinction between diffractive and inelastic DIS. Our considerations can readily be extended to the spectrum of soft quarks, $\mathbf{p}^2 \lesssim Q_A^2$, in hard photons, $Q^2 \gtrsim Q_A^2$. In this case, the result (21) for diffractive DIS is retained, whereas in the numerator of the result (22) for truly inelastic DIS, one must substitute $Q^2 \longrightarrow Q_A^2$ so that in this case $dq_{FS}|_D \approx dq_{FS}|_{\rm in}$ and $dq_{IS} \approx 2dq_{FS}|_D$. The evolution of a soft nuclear sea, $\mathbf{p}^2 \lesssim Q_A^2$, is entirely driven by an anti-collinear splitting of the NSS-defined WW nuclear glue into the sea partons.

The early discussion of the FS quark density in the saturation regime is due to Mueller [14]. Mueller focused on $Q^2 \gg Q_A^2$ and discussed neither a distinction between diffractive and truly inelastic DIS nor a $Q^2$ dependence and broadening (15) for truly inelastic DIS at $Q^2 \lesssim Q_A^2$.

We come to a summary. We reported a derivation of the FS parton density. Our result (9) summarizes in an elegant way intranuclear distortions due to multiple diffractive rescatterings and color excitations of the target nucleus. In conjunction with the NSS definition of the WW glue of the nucleus, Eqs. (11) and (12) give an explicit form of the FS parton densities. The two-plateau FS quark density with the strong $Q^2$ dependence of the plateau for truly inelastic DIS has not been discussed before. A comparison with the IS nuclear parton densities which evolve from the NSS-defined WW nuclear glue shows an exact equality of the FS and IS parton densities. The plateau-like saturated nuclear quark density is suggestive of Fermi statistics, but our principal point that for any projectile which interacts weakly with colored partons the saturated density measures the momentum distribution in the $q\bar{q}$, $gg$, … Fock state of the projectile disproves the Fermi-statistics interpretation. The spin and color multiplet of colored partons the photon couples to is completely irrelevant, what only counts is an opacity of heavy nuclei. The anti-collinear splitting of WW nuclear glue into soft sea partons is a noteworthy feature of both diffractive DIS and IS sea parton distributions. The emergence of a saturated density of IS sea partons from the nuclear-diluted WW glue is due to the nuclear broadening of the plateau (15). Because the predominance of diffraction is a very special feature of DIS [5], one must be careful with applying the IS parton densities to, for instance, nuclear collisions, in which diffraction would not be of any significance.

One can go one step further and consider interactions with the opaque nucleus of the $q\bar{q}\,g$ Fock states of the photon. Then the above analysis can be extended to $x \ll x_A$, and the issue of the $x$-dependence of the saturation scale $Q_A^2$ can be addressed following the discussion in [9]. We only mention here that as far as diffraction and IS parton densities are concerned, the NSS-defined WW glue remains a useful concept, and the close correspondence between $\phi_{WW}(\boldsymbol{\kappa})$ for the nucleus and $f(\boldsymbol{\kappa})$ for the nucleon is retained.

This work was partially supported by the INTAS grants (project nos. 97-30494 and 00-00366) the DFG grant (project no. 436RUS17/119/01) and by DAAD and Nordita.

## REFERENCES

1. N. N. Nikolaev and V. I. Zakharov, Yad. Fiz. **21**, 434 (1975) [Sov. J. Nucl. Phys. **21**, 227 (1975)]; Phys. Lett. B **55B**, 397 (1975).
2. A. H. Mueller, Nucl. Phys. B **335**, 115 (1990).
3. L. McLerran and R. Venugopalan, Phys. Rev. D **49**, 2233 (1994); **55**, 5414 (1997); E. Iancu, A. Leonidov, and L. McLerran, *Lectures at the Cargése Summer School, 2001*, hep-ph/0202270.
4. N. N. Nikolaev, W. Schäfer, and G. Schwiete, Pis'ma Zh. Éksp. Teor. Fiz. **72**, 405 (2000) [JETP Lett. **72**, 583 (2000)]; Phys. Rev. D **63**, 014020 (2001).

5. N. N. Nikolaev, B. G. Zakharov, and V. R. Zoller, Z. Phys. A **351**, 435 (1995).
6. M. Genovese, N. N. Nikolaev, and B. G. Zakharov, Zh. Éksp. Teor. Fiz. **108**, 1155 (1995) [JETP **81**, 633 (1995)].
7. N. N. Nikolaev and B. G. Zakharov, Z. Phys. C **49**, 607 (1991).
8. N. N. Nikolaev and B. G. Zakharov, Z. Phys. C **53**, 331 (1992).
9. N. N. Nikolaev and B. G. Zakharov, Zh. Éksp. Teor. Fiz. **105**, 1498 (1994) [JETP **78**, 806 (1994)]; Z. Phys. C **64**, 631 (1994).
10. N. N. Nikolaev, B. G. Zakharov, and V. R. Zoller, Pis'ma Zh. Éksp. Teor. Fiz. **59**, 8 (1994) [JETP Lett. **59**, 6 (1994)].
11. N. N. Nikolaev, Zh. Éksp. Teor. Fiz. **81**, 814 (1981) [Sov. Phys. JETP **54**, 434 (1981)].
12. N. N. Nikolaev and B. G. Zakharov, Phys. Lett. B **332**, 177 (1994).
13. M. Genovese, N. N. Nikolaev, and B. G. Zakharov, Phys. Lett. B **378**, 347 (1996).
14. A. H. Mueller, Nucl. Phys. B **558**, 285 (1999); *Lectures at the Cargése Summer School, 2001*, hep-ph/0111244.

JETP Letters, Vol. 76, No. 4, 2002, pp. 201–205. From Pis'ma v Zhurnal Éksperimental'noĭ i Teoreticheskoĭ Fiziki, Vol. 76, No. 4, 2002, pp. 236–240.


# Coherent Final State Interaction in Jet Production in Nucleus–Nucleus Collisions¶

**B. G. Zakharov**

*Landau Institute for Theoretical Physics, Russian Academy of Sciences, Moscow, 117940 Russia*

Received July 18, 2002

The coherent final state interaction of an energetic parton produced in *AA* collisions is studied. This interaction is due to the change in the cutoff scale and in the running coupling constant when the parton passes from a vacuum to a quark–gluon plasma. It is demonstrated that the contribution of this new mechanism to the energy loss may be of the same order of magnitude as the induced gluon radiation. However, an accurate evaluation of this medium effect is a difficult task, because there is a strong cancellation between the cutoff and running coupling constant effects. The uncertainties in the contribution of the coherent final state interaction restrict strongly the accuracy of jet tomographic analyses of the matter density produced in *AA* reactions. © *2002 MAIK "Nauka/Interperiodica"*.

PACS numbers: 24.85.+p; 25.75.Dw

**1. Introduction.** In recent years there has been much work done on the energy loss of fast partons in a hot QCD medium due to gluon radiation induced by multiple scattering (for a review, see [1]). This is of great importance for understanding the final state interaction in hard reactions in high energy nucleus–nucleus collisions, which are under active investigation at RHIC and will be studied in future experiments at LHC.

Theoretical calculations show that the energy loss in quark–gluon plasma (QGP) considerably exceeds that in hadronic medium [2–4]. Since gluon radiation softens the parton fragmentation functions of energetic partons produced in hard reactions in the initial stage of *AA* collisions it should lead to significant suppression of the high $p_T$ hadronic spectra in *AA* collisions with respect to *pp* collisions (so-called jet quenching) if a hot QGP is formed [5, 6]. Such suppression was indeed recently discovered by the PHENIX experiment [7] at RHIC for $\pi^0$ spectra at $p_T \lesssim 4$ GeV in central Au + Au collisions at $\sqrt{s}$ = 130 GeV. Because the energy loss is sensitive to the density of the hot medium, it looks quite natural to use experimental data on high $p_T$ spectra for jet tomographic analysis of the matter density produced in *AA* reactions [8–10].

To understand the range of uncertainty in jet tomographic analyses, it is important to study the other possible final state interaction effects in jet production. One mechanism of potential interest is the in-medium modification of the parton cascade without gluon exchanges between the fast partons and thermal partons (I call this mechanism the coherent final state interaction (CFSI)). The reason is evident: jet splitting in vacuum is the major mechanism of the energy loss of energetic partons, and if the medium affects the parton cascading, one can expect a significant modification of the fragmentation functions. For example, such a modification should inevitably arise as a mass effect due to different infrared cutoff scales in a vacuum and a QGP. Another obvious source of the CFSI is the in-medium modification of the running coupling constant[1] $\alpha_s(k)$. Although at large virtualities the running coupling constants in the vacuum and QGP are close to each other, this should not be the case at low $k$, where different background environments in which the gluon bremsstrahlung occurs can lead to a difference in the running coupling constants in these two cases. Note that both these medium effects should lead to transition radiation very similar to that of photon radiation in QED. The purpose of the present work is to address the CFSI for RHIC conditions within a simple model for gluon radiation, which will be discussed in detail below.

**2. Cutoff scales and running coupling constants.** Let us first discuss the magnitudes of the cutoff scales for parton splitting in a vacuum and QGP. In a QCD vacuum, the natural cutoff is the inverse gluon correlation radius $R_c^{-1} \sim 0.8$–1 GeV [11, 12]. At such a virtuality scale, the perturbative cascade stops in Monte Carlo programs like JETSET, and string fragmentation takes over. Note also that the introduction of the effective gluon mass $m_{g,v} \sim R_c^{-1}$ (hereafter I use the index $v$ for vacuum quantities, and for the plasma quantities below I use the index $p$) allows one to describe the HERA data on the low-$x$; proton structure function

¶This article was submitted by the author in English.

[1] Note that these CPSI effects differ from the coherent double gluon exchanges which are usually included in the induced gluon radiation to insure the unitarity [3].

[13]. The analysis of inclusive radiative decays of the $J/\Psi$ and $\Upsilon$ [14] also gives $m_{g,v} \sim 0.7$–$1.2$ GeV.

In the QGP phase, the nonperturbative fluctuations are suppressed, and the natural cutoff for radiation of transverse gluons, which propagate through QGP as quasiparticles, is the thermal gluon mass. At high temperature, it reads $m_{g,p}^2 = (g^2T^2/2)(N_c/3 + N_f/6)$. An analysis of the results of lattice calculations shows that in the temperature range $T \sim (1$–$3)T_c$ ($T_c \approx 170$ MeV is the temperature of the confinement phase transition), which is of relevance to *AA* collisions at RHIC, the nonperturbative effects are still important [15]. Using a quasiparticle picture with massive gluons and quarks in the above temperature window, the authors of [15] obtained $m_{g,p} \approx 0.4$ GeV, and $m_{q,p} \approx 0.3$ GeV. Thus, I see that there is a considerable difference in the cutoffs in a vacuum and a QGP.

Let us recall now the situation with the running coupling constant at low $k$. There are some indications that in the vacuum nonperturbative effects stop the growth of the running coupling constant at $k \lesssim k_c \sim 1$ GeV [16–19]. Phenomenologically, the magnitude of $\alpha_{s,v}$ at $k \lesssim k_c$ can be estimated from, say, an analysis of heavy quark energy losses, which gives [17]

$$\int_0^{2\ \mathrm{GeV}} dk \frac{\alpha_{s,v}(k)}{\pi} \approx 0.36\ \mathrm{GeV}. \qquad (1)$$

For the simplest prescription with frozen $\alpha_{s,v}$ at $k < k_c$ (the so-called *F*-model [17]), using the one-loop expression at $k > k_c$, one can obtain from Eq. (2) $\alpha_{s,v}(k < k_c) = \alpha_{s,v}^{fr} \approx 0.7$, and $k_c \approx 0.82$ GeV. These values are for $\Lambda_{QCD} = 0.3$ GeV.

Unfortunately, at present, there is no accurate information on $\alpha_s(k)$ for gluon emission from a fast parton in a QGP. Available pQCD calculations are performed in the static limit (see, for example, [20–22] and references therein). The running coupling constant obtained in [21, 22] has a pole at $k/\Lambda_{QCD} \sim 3$ at $T \sim 250$ MeV. Thus, in pQCD, even for the static case, the situation with the $k$-dependence of the in-medium running coupling constant at low $k$ is unclear. On the other hand, an analysis of lattice results within the quasiparticle model gives the thermal $\alpha_s$ with a smooth $T$-dependence, and at $T \sim 250$ MeV $\alpha_s \approx 0.5$ [15]. In the present paper, in the absence of accurate information on the in-medium running coupling constant for fast partons, I perform calculations using the above *F*-model with different values of $\alpha_{s,p}^{fr}$.

**3. Evaluation of the coherent medium correction to the gluon spectrum.** Let us now discuss the technical aspects of our analysis of CPSI. I consider the gluon radiation from a fast quark (the generalization to the radiation from a gluon is trivial). I neglect multiple emission and consider only the leading order splitting $q \longrightarrow gq$. This is reasonable, since the effect is dominated by the gluons with small transverse momenta $k \lesssim$ 1–2 GeV. Note that I choose the $z$-axis along the momentum of the initial fast parton, so for the central rapidity region in *AA* collisions our $L$ is the ordinary transverse distance between the jet production point and the boundary of QGP.

I consider a fast quark with energy $E_i$ produced at $z = 0$, which eventually splits at some $z > 0$ into a gluon and a final quark with energies $E_g = xE_i$ and $E_f = (1 - x)E_i$, respectively. The corresponding matrix element can be written in the form (below, for simplicity, I drop color factors)

$$T = i\int_0^\infty dz \int d\boldsymbol{\rho} g \bar{\psi}_f(\boldsymbol{\rho}, z)\gamma^\mu A_\mu(\boldsymbol{\rho}, z)\psi_i(\boldsymbol{\rho}, z), \qquad (2)$$

where $\psi_{i,f}(z, \boldsymbol{\rho})$ are the wave functions of the initial and final quarks, $A_\mu$ is the wave function of the emitted gluon, and $\boldsymbol{\rho}$ is the transverse coordinate. In Eq. (2), I do not explicitly indicate the $z$ and $k$ dependence of the running coupling constant $g$. I evaluate the matrix element in Eq. (2) for small emission angles. Then, at high energies $E_j \gg m_q$, the quark wave functions using the ordinary light-cone spinor basis can be written as

$$\psi_j(\boldsymbol{\rho}, z) = \exp(iE_j z)\hat{U}_j \phi_j(z, \boldsymbol{\rho}), \qquad (3)$$

where the operator $\hat{U}_j$ is

$$\hat{U}_j = \left(\sqrt{2E_j} + \frac{\boldsymbol{\alpha}\boldsymbol{\rho} + \beta m_q}{\sqrt{2E_j}}\right)\chi_j. \qquad (4)$$

Here, $\chi_j$ is the quark spinor (normalized to unity), $\boldsymbol{\alpha} = \gamma^0\boldsymbol{\gamma}$, $\beta = \gamma^0$, and $\mathbf{p} = -i\nabla_\perp$. The gluon wave function can be written in a form similar to Eq. (3) (up to an obvious change of the spin operator). The transverse quark wave function $\phi_j(\boldsymbol{\rho}, z)$ entering into Eq. (3) is governed by the two-dimensional Schrödinger equation in which $z$ plays the role of time

$$i\frac{\partial \phi_j(z, \boldsymbol{\rho})}{\partial z} = \frac{(\mathbf{p}^2 + m_q^2)}{2E_j}\phi_j(z, \boldsymbol{\rho}). \qquad (5)$$

A similar equation holds for the gluon wave function.

Without a loss of generality, I can take for the initial quark the plane wave state in the $\boldsymbol{\rho}$-plane and set $\mathbf{p}_i = 0$. Then all the transverse wave functions can be written as

$$\phi_j(z, \boldsymbol{\rho}) = \exp\left\{i\left[\mathbf{p}_j\boldsymbol{\rho} - \int_0^z d\xi \frac{(\mathbf{p}_j^2 + m_j^2(\xi))}{2E_j}\right]\right\}. \qquad (6)$$

Eventually, the $\boldsymbol{\rho}$-integration in Eq. (2) will give $\mathbf{p}_g + \mathbf{p}_f = \mathbf{p}_i = 0$. Note that, since the quark mass is of only marginal significance (for light quarks) in the gluon radiation, I will neglect the $z$ dependence of $m_q$ and use the same quark mass in a vacuum and in a QGP. How-

ever, for the gluon transverse wave function, I use the $z$-dependent gluon mass: $m_g(z < L) = m_{g,p}$ and $m_g(z > L) = m_{g,v}$. Using the above equations for the transition amplitude and wave functions, with the help of the standard Fermi golden rule, one can obtain after some simple calculations for the gluon distribution (below $\mathbf{k} = \mathbf{p}_g$)

$$\frac{dN}{dxd\mathbf{k}^2} = \frac{dN^{(0)}}{dxd\mathbf{k}^2} + \frac{dN^{(1)}}{dxd\mathbf{k}^2}, \tag{7}$$

$$\frac{dN^{(0)}}{dxd\mathbf{k}^2} = \frac{C_F\alpha_s^v(k)}{\pi x}\left(1 - x + \frac{x^2}{2}\right)\frac{\mathbf{k}^2}{(\mathbf{k}^2 + \mu_v^2)^2}, \tag{8}$$

$$\frac{dN^{(1)}}{dxd\mathbf{k}^2} = \frac{2C_F\alpha_s^v(k)}{\pi x}\left(1 - x + \frac{x^2}{2}\right)$$

$$\times\left[1 - \cos\left(\frac{(\mathbf{k}^2 + \mu_p^2)L}{2E_i x(1-x)}\right)\right] \tag{9}$$

$$\times\frac{\mathbf{k}^2 r(k)[(r(k)-1)\mathbf{k}^2 + r(k)\mu_v^2 - \mu_p^2]}{(\mathbf{k}^2 + \mu_p^2)^2(\mathbf{k}^2 + \mu_v^2)},$$

where $\mu_i^2 = m_q^2 x^2 + m_{g,i}^2(1 - x)$, $r(k) = \sqrt{\alpha_{s,p}(k)/\alpha_{s,v}(k)}$. The first term on the r.h.s of (7) is the gluon spectrum in a vacuum, and the second one gives the medium correction of interest. In deriving Eqs. (8) and (9), I neglected the small spin-flip contribution ($\propto m_q^2$).

Recall that the gluon formation length is $L_f \sim 2E_i x(1-x)/(\mathbf{k}^2 + \mu^2)$ (I do not specify here the medium index, since $\mu_p$ and $\mu_v$ are of the same order). Thus, it is seen that the argument of cosine in the r.h.s. of (9) is $\sim L/L_f$. Obviously, at $L_f \ll L$, the rapidly oscillating cosine as a function of $L$ will vanish upon averaging over the production point of the fast quark, and one gets an $L$-independent correction to the vacuum term. It can be written in the following physically transparent form

$$\left.\frac{dN^{(1)}}{dxd\mathbf{k}^2}\right|_{L_f \ll L} \approx \left.\frac{dN^{(0)}}{dxd\mathbf{k}^2}\right|_p - \left.\frac{dN^{(0)}}{dxd\mathbf{k}^2}\right|_v + \frac{dN^{\text{tran}}}{dxd\mathbf{k}^2}, \tag{10}$$

where the first two terms simply describe the modification of the spectrum due to the change in $m_g$ and $\alpha_s$ (in an infinite QGP), and the last term is the contribution of the transition radiation which reads

$$\frac{dN^{\text{tran}}}{dxd\mathbf{k}^2} = \frac{C_F\alpha_s^v(k)}{\pi x}\left(1 - x + \frac{x^2}{2}\right)\left(\frac{\mathbf{k}r(k)}{\mathbf{k}^2 + \mu_p^2} - \frac{\mathbf{k}}{\mathbf{k}^2 + \mu_v^2}\right). \tag{11}$$

It can be derived from (2) taking $-\infty$ for the lower limit of the $z$ integral. Note that the changes in both $m_g$ and $\alpha_s$ cause the transition radiation.

On the other hand, for the gluons with $L_f \gg L$, expanding cosine in (9), one gets the correction $\propto L^2$

$$\left.\frac{dN^{(1)}}{dxd\mathbf{k}^2}\right|_{L_f \gg L} \approx \frac{C_F\alpha_s(k)L^2}{\pi x}\left(1 - x + \frac{x^2}{2}\right)$$

$$\times\frac{\mathbf{k}^2 r(k)[(r(k)-1)\mathbf{k}^2 + r(k)\mu_v^2 - \mu_p^2]}{4E_i^2 x^2(1-x)^2(\mathbf{k}^2 + \mu_v^2)}. \tag{12}$$

In this regime one cannot separate the transition radiation. The above relationships demonstrate that the decrease in the cutoff and that in the coupling constant in QGP work in opposite directions. One can also see that the relative contribution of the medium correction in Eq. (7) is larger for gluons with $L_f \lesssim L$. These facts are consistent with intuitive expectations.

**4. Numerical results.** In numerical calculations, I take $m_{g,v} = 0.4$ and $m_{g,v} = 0.8$ GeV, and for the quark mass, I take $m_{q,p} = m_{q,v} = 0.3$ GeV. As was mentioned above in the absence of accurate data on the in-medium $\alpha_s$ at low $k$, I perform numerical calculations parametrizing it in the same $F$-model as for $\alpha_{s,v}$ for several values of $\alpha_{s,p}^{fr}$. To understand the sensitivity of CFSI to $\alpha_{s,p}^{fr}$ I use for it four values: 0.7, 0.5, 0.4, and 0.3. The first version, corresponding to $\alpha_{s,p} = \alpha_{s,v}$, is unlikely to be realistic, since it neglects the in-medium modification of $\alpha_s(k)$, but it allows one to see the magnitude of the purely mass effect. The last value is also unlikely to be realistic. Indeed, the results of the analysis of the lattice data within the quasiparticle QGP model [15] say that $\alpha_s \approx 0.3$ occurs for $T \approx 2.2T_c$. Since a QGP can have a temperature above this value only within a short time interval, in the initial stage of its evolution, the value of $\alpha_{s,p}^{fr} = 0.3$ is probably too small for the evaluation of the CFSI. The value $\alpha_{s,p}^{fr} = 0.5$ seems to be most reasonable. For instance, it is close to the value $\alpha_s \approx 0.47$ obtained in [15] at $T \approx 1.5T_c \approx 250$ MeV. Of course, it is not obvious that the thermal $\alpha_s$s can be extrapolated safely to higher energies. However, one can expect that in the splitting of fast partons, the thermal bath effect on $\alpha_s$ can only be weaker than that for the thermal partons. If this is the case, the CFSI correction may be larger than our estimate.

In Fig. 1, I show the $x$ dependence of the ratio $R(x) = \frac{dN}{dx}/\frac{dN^{(0)}}{dx}$ for several $k$ windows at $E_i = 40$ GeV averaged over $L$ in the interval [0, 6] fm. As can be seen in Fig. 1, for $\alpha_{s,p} = \alpha_{s,v}$ the mass effect alone enhances considerably the probability of gluon emission at low $x$ and $k \lesssim 1$ GeV. The curves for smaller values of $\alpha_{s,p}^{fr}$

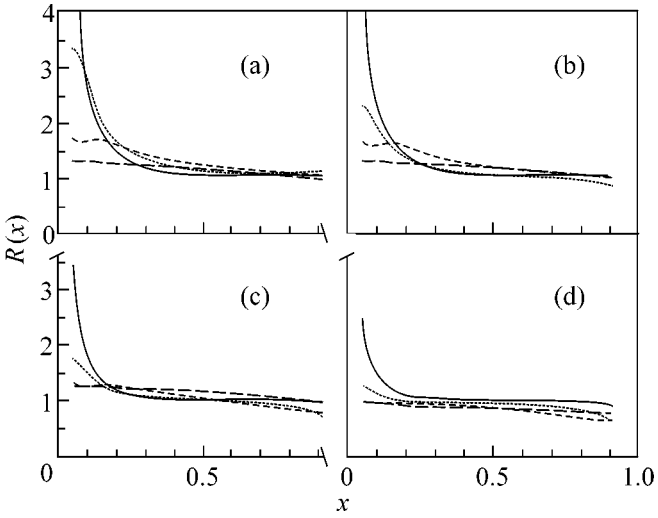


**Fig. 1.** The ratio $R(x) = \frac{dN}{dx} / \frac{dN^{(0)}}{dx}$ at $E_i$ = 40 GeV for $\alpha_{s,p}^{fr}$ = (a) 0.7, (b) 0.5, (c) 0.4, and (d) 0.3 evaluated using Eqs. (7)–(9) for the *k*-windows: [0, 0.5] (solid line), [0.5, 1] (dotted line), [1, 1.5] (dashed line), and [1.5, 2] (long dashed line) GeV. The *x*-distributions were obtained by averaging over *L* in the interval [0, 6] fm.

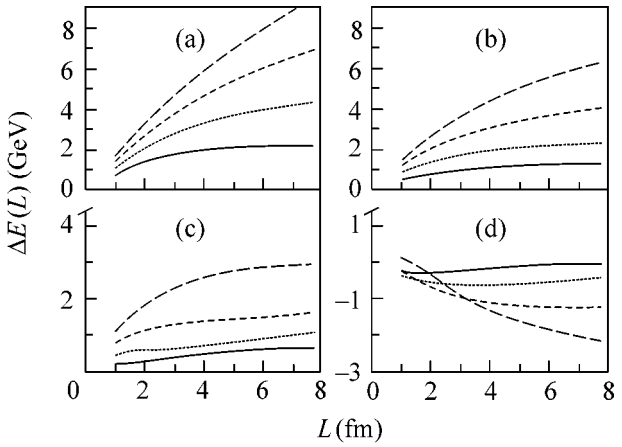


**Fig. 2.** The quark energy loss Δ*E* due to the CFSI as a function of *L* for $\alpha_{s,p}^{fr}$ = (a) 0.7, (b) 0.5, (c) 0.4, and (d) 0.3 at $E_i$ = 10 (solid line), 20 (dotted line), 40 (dashed line), and 80 (long dashed line) GeV.

show that the enhancement of radiation due to the smaller cutoff in a QGP is strongly compensated by the effect of the smaller coupling constant in a QGP, and for the probably unrealistic $\alpha_{s,p}^{fr} = 0.3$, there is a kinematic region where CFSI suppresses the gluon radiation. Using (9), I also calculated the energy loss, defined as

$$\Delta E = E_i \int_{x_{\min}}^{x_{\max}} dx \int_0^{k^2_{\max}} d\mathbf{k}^2 x \frac{dN^{(1)}}{dx d\mathbf{k}^2}.$$

For the limits of the $x$ and $\mathbf{k}^2$ integration, I take $x_{\min} = m_g/E_i$, $x_{\max} = m_q/E_i$, and $k^2_{\max} = \min[E_i^2 x^2, E_i^2 (1-x)^2]$. In Fig. 2, I show the results for Δ*E* as a function of *L* at $E_i$ = 10, 20, 40, and 80 GeV. As one can see, for $\alpha_{s,p}^{fr}$ = 0.7, 0.5, and 0.4, the energy loss is positive, rising with *L* and $E_i$. For $\alpha_{s,p}^{fr} = 0.3$ Δ*E* becomes negative, which shows that the suppression of the gluon radiation due to the small coupling constant becomes stronger than the enhancement caused by the mass effect. This strong cancellation between the two competing effects makes it difficult to make definitive predictions for the effect of CFSI in the region $\alpha_{s,p}^{fr} \sim 0.3$–0.4. Note that our Δ*E* for $\alpha_{s,p}^{fr} = 0.5$ appears to be of the same order of magnitude as the GLV predicted in [8] for the energy loss due to the induced radiation.

**5. Summary.** I have shown that the final state interaction due to the change in the cutoff scale and in the running coupling constant when the parton passes from a vacuum to a QGP modifies the gluon radiation from fast partons produced in *AA* collisions. The contribution of this mechanism to the energy loss can be of the same order of magnitude as the induced gluon radiation. However, an accurate evaluation of the CFSI is a difficult task, since there are strong cancellations between the mass and running coupling constant effects, and the results depend strongly on the assumptions on the *k* dependence of the in-medium $\alpha_s(k)$.

The results of the present paper raise a practical question of whether the jet tomographic analyses based on the theory of induced gluon radiation can be used for extracting the density of a hot QCD medium produced in *AA* collisions. At present, one cannot exclude the possibility that the CFSI may appear to be even more important than the induced radiation. To clarify the situation, it is highly desirable to study the influence of QGP on the running coupling constant for fast partons.

I am grateful to R. Baier and N.N. Nikolaev for discussions. I am also grateful to J. Speth for the hospitality at FZJ, Jülich, where this work was completed. This work was partially supported by INTAS (project no. 97-30494) and DFG (project no. 436RUS17/119/01).

## REFERENCES

1. R. Baier, D. Schiff, and B. G. Zakharov, Annu. Rev. Nucl. Part. Sci. **50**, 37 (2000).
2. R. Baier *et al.*, Nucl. Phys. B **483**, 291 (1997); **484**, 265 (1997); **531**, 403 (1998); JHEP **0109**, 033 (2001).
3. B. G. Zakharov, Pis'ma Zh. Éksp. Teor. Fiz. **63**, 906 (1996) [JETP Lett. **63**, 952 (1996)]; Pis'ma Zh. Éksp. Teor. Fiz. **65**, 585 (1997) [JETP Lett. **65**, 615 (1997)];

Pis'ma Zh. Éksp. Teor. Fiz. **70**, 181 (1999) [JETP Lett. **70**, 176 (1999)]; Yad. Fiz. **61**, 924 (1998) [Phys. At. Nucl. **61**, 838 (1998)]; hep-ph/9807396.

4. M. Gyulassy, P. Levai, and I. Vitev, Nucl. Phys. B **594**, 371 (2001).
5. X.-N. Wang, Phys. Rev. C **58**, 2321 (1998).
6. I. P. Lokhtin and A. M. Snigirev, Phys. Lett. B **440**, 163 (1998).
7. K. Adcox *et al.* (PHENIX Collab.), Phys. Rev. Lett. **88**, 022301 (2002).
8. M. Gyulassy, P. Levai, and I. Vitev, Phys. Lett. B **538**, 282 (2002).
9. C. S. Salgado and U. A. Wiedemann, hep-ph/0204221 (2002).
10. E. Wang and X.-N. Wang, hep-ph/0202105 (2002).
11. E. V. Shuryak, Rev. Mod. Phys. **65**, 1 (1993).
12. E. V. Shuryak, hep-ph/0205031 (2002).
13. N. N. Nikolaev and B. G. Zakharov, Phys. Lett. B **327**, 149 (1994).
14. J. H. Field, hep-ph/0101158 (2002).
15. P. Levai and U. Heinz, Phys. Rev. C **57**, 1879 (1998).
16. A. C. Mattingly and P. M. Stevenson, Phys. Rev. D **49**, 437 (1994).
17. Yu. L. Dokshitzer, V. A. Khoze, and S. I. Troyan, Phys. Rev. D **53**, 89 (1996).
18. Yu. L. Dokshitzer, G. Marchesini, and B. R. Webber, Nucl. Phys. B **469**, 93 (1996).
19. D. V. Shirkov and I. L. Solovtsov, Phys. Rev. Lett. **79**, 1209 (1997).
20. R. Baier, B. Pire, and D. Schiff, Phys. Lett. B **238**, 367 (1990).
21. M. A. van Eijick, C. R. Stephens, and Ch. G. van Weert, Mod. Phys. Lett. A **9**, 309 (1994).
22. M. Chaichian and M. Hayashi, Acta Phys. Pol. **27**, 1703 (1996).

JETP Letters, Vol. 76, No. 4, 2002, pp. 206–210. Translated from Pis'ma v Zhurnal Éksperimental'noĭ i Teoreticheskoĭ Fiziki, Vol. 76, No. 4, 2002, pp. 241–245.


# Self-Division of a Pulse Consisting of Several Light-Field Oscillations in a Nonlinear Medium with Dispersion

**S. A. Kozlov* and P. A. Petroshenko**

*Institute of Fine Mechanics and Optics, ul. Sablinskaya 14, St. Petersburg, 197101 Russia*

** e-mail: kozlov@phd.ifmo.ru*

Received June 8, 2002

The nonparaxial dynamics of light pulses consisting of several light-field oscillations in nonlinear media with dispersion is analyzed. It is shown that the self-action of these extremely short pulses can result in their self-division. © *2002 MAIK "Nauka/Interperiodica".*

PACS numbers: 42.65.Jx

The investigation of the self-action of light pulses consisting of several light-field oscillations is at the front line of nonlinear optics of ultrashort pulses [1]. The envelope concept is physically meaningless for these extremely short pulses. Being derived in the approximation of quasi-monochromatic radiation, the equations of envelope motion [2, 3], which are customary for nonlinear optics, are invalid for these pulses. The theory of the nonlinear propagation of extremely short pulses through various media was developed in numerous studies and is usually based on equations describing the dynamics of the pulse field rather than envelope (e.g., see [4, 5]). In most of these papers, the nonlinear evolution of the field of an extremely short pulse with a stationary transverse structure was analyzed (which is assumed to be true in the first approximation in waveguides). The papers that consider the variation of the transverse spatial distribution of the field of extremely short pulses (in 3D nonlinear media) are considerably fewer in number. These papers are usually devoted to the paraxial evolution of extremely short pulses. In particular, a method for deriving the paraxial-diffraction equations for extremely short pulses was formulated in [6], the equations describing the paraxial dynamics of the field of an extremely short pulse in a nonlinear dielectric medium with dispersion were presented in [7], and the solutions of these equations were simulated numerically in [8]. However, the consistent theory of the self-action of extremely short pulses must be nonparaxial. It is reasonable to analyze the propagation of light pulses whose transverse size is commensurable with the central wavelength allowing for possible changes in the transverse structure of the field on the same scale [8].

In this paper, the nonparaxial evolution of extremely short pulses is described by the spectral analysis method. It was this approach that was used in [9] to derive the truncated equation for the nonparaxial self-focusing of monochromatic radiation. The spectral approach proposed in [9] is generalized here to radiation with a wide time spectrum. A new truncated equation describing the nonparaxial dynamics of the spatial spectrum of extremely short pulses in a homogeneous isotropic dielectric medium with an arbitrary spectral dependence of the linear refractive index and nonresonant electron nonlinearity was derived. We obtain the solutions of this equation, which demonstrate the self-division of an extremely short pulse in the process of the self-broadening of its spectrum.

For light radiation propagating through a dielectric medium, the Maxwell equations reduce to the form [10]

$$\nabla \times (\nabla \times \mathbf{E}) + \frac{1}{c^2}\frac{\partial^2 \mathbf{E}}{\partial t^2} + \frac{4\pi}{c^2}\frac{\partial^2 \mathbf{P}}{\partial t^2} = 0, \qquad (1)$$

where **E** is the electric field of a source, **P** is the medium polarization, $c$ is the speed of light in vacuum, $t$ is the time, and $\nabla$ is the gradient operator.

In this paper, we analyze only the scalar problem of the self-action of a two-dimensional beam of *TE* polarized radiation. The direction of radiation propagation is referred to as the $z$ axis, $x$ is the transverse coordinate, and the $y$ axis is the direction of the linearly polarized electric field of radiation. The dielectric medium through which extremely short pulses propagate is considered as a homogeneous and isotropic medium where the linear refractive index $n(\omega)$ is an arbitrary function of the frequency $\omega$. The nonlinear component of medium polarization is taken in the simplest form $P_{nl} = \chi E^3$, where $\chi$ is the nonlinear susceptibility. This representation of the nonlinear response of a dielectric material in the field of an extremely short pulse is well justified in the first approximation if the response is nonresonant and has the electronic origin [5]. The virtually inertialess character of the nonresonant nonlinearity of dielectric materials in the field of ultrashort laser pulses is corroborated by the weak dispersion of their nonlin-

0021-3640/02/7604-0206$22.00 

ear refractive index in a considerable part of the transparency ranges of these materials [11]. Under the above assumptions, Eq. (1) for the frequency spectrum of radiation

$$G(z, x, \omega) = \int_{-\infty}^{+\infty} E(z, x, t)e^{-i\omega t}dt$$

can be written in the form

$$\frac{\partial^2 G}{\partial z^2} + \frac{\partial^2 G}{\partial x^2} + \frac{\omega^2 n^2(\omega)}{c^2}G + \frac{\chi\omega^2}{\pi c^2}\int_{-\infty}^{+\infty}\int_{-\infty}^{+\infty} G(\omega-\alpha)G(\alpha-\beta)G(\beta)d\alpha d\beta = 0, \quad (2)$$

which, in turn, for the spatial spectrum

$$g(z, k_x, \omega) = \int_{-\infty}^{+\infty} G(z, x, \omega)e^{-ik_x x}dx,$$

takes the form

$$\frac{\partial^2 g}{\partial z^2} + \left(\frac{\omega^2 n^2(\omega)}{c^2} - k_x^2\right)g + \frac{\chi\omega^2}{4\pi^3 c^2}\int_{+\infty}^{-\infty}\int\int\int g(k_x - m_x - n_x, \omega-\alpha) \times g(m_x, \alpha-\beta)g(n_x, \beta)dm_x dn_x d\alpha d\beta = 0. \quad (3)$$

Equations (2) and (3) describe both the propagation of light waves in the positive and negative $z$ directions and their interaction due to medium nonlinearity. Let us derive the equation of the unidirectional propagation of radiation.

Linearized Eq. (3) has the solution

$$g(z, k_x, \omega) = C_1(k_x, \omega)e^{-i\frac{\omega n(\omega)}{c}\sqrt{1-\frac{k_x^2c^2}{\omega^2n^2(\omega)}}z} + C_2(k_x, \omega)e^{i\frac{\omega n(\omega)}{c}\sqrt{1-\frac{k_x^2c^2}{\omega^2n^2(\omega)}}z}, \quad (4)$$

where $C_1$ and $C_2$ are the integration constants. The first and second terms describe the diffraction of direct and inverse waves, respectively. Equation (4) indicates that the nonparaxial diffraction of the direct wave ($C_2 = 0$) is described by the truncated linear equation

$$\frac{\partial g}{\partial z} + i\frac{\omega n(\omega)}{c}\sqrt{1-\frac{k_x^2c^2}{\omega^2n^2(\omega)}}g = 0. \quad (5)$$

Let us generalize Eq. (5) to the nonlinear propagation of radiation. We will seek the truncated nonlinear equation in the form

$$\frac{\partial g}{\partial z} + i\frac{\omega n(\omega)}{c}\sqrt{1-\frac{k_x^2c^2}{\omega^2n(\omega)}}g + \chi N(g) = 0, \quad (6)$$

where $N(g)$ is the unknown nonlinear operator.

The change from linearized Eq. (3) to truncated Eq. (5) (with lower $z$ derivative) physically means the change to an analysis of unidirectional-wave diffraction. A solution of truncated Eq. (5) is obviously a particular solution of linearized total Eq. (3). In order to determine the form of the operator $N(g)$ in Eq. (6), we require that solutions of truncated Eq. (6) are solutions of total Eq. (3). According to the procedure proposed in [9], differentiating Eq. (6) in $z$ and expressing $\partial g/\partial z$ in terms of $g$ from the same E, we obtain

$$\frac{\partial}{\partial z}\left(\frac{\partial g}{\partial z} + i\frac{\omega n(\omega)}{c}\sqrt{1-\frac{k_x^2c^2}{\omega^2n^2(\omega)}}g + \chi N(g)\right) = \frac{\partial^2 g}{\partial z^2} + \left(\frac{\omega^2 n^2(\omega)}{c^2} - k_x^2\right)g - i\frac{\omega n(\omega)}{c}\sqrt{1-\frac{k_x^2c^2}{\omega^2n^2(\omega)}}\chi N(g) + \chi\frac{\partial}{\partial z}N(g) = 0. \quad (7)$$

Comparing Eqs. (7) and (3), we arrive at the following relation for the operator $N(g)$:

$$-i\frac{\omega n(\omega)}{c}\sqrt{1-\frac{k_x^2c^2}{\omega^2n^2(\omega)}}N(g) + \frac{\partial}{\partial z}N(g) = \frac{\chi\omega^2}{4\pi^3c^2}\int_{+\infty}^{-\infty}\int\int\int g(k_x - m_x - n_x, \omega-\alpha) \times g(m_x, \alpha-\beta)g(n_x, \beta)dm_x dn_x d\alpha d\beta. \quad (8)$$

We seek $N(g)$ in the form

$$N(g) = \int_{-\infty}^{+\infty}\int\int\int\Phi(k_x, \omega, m_x, n_x, \alpha, \beta) \times g(k_x - m_x - n_x, \omega-\alpha)g(m_x, \alpha-\beta) \times g(n_x, \beta)dm_x dn_x d\alpha d\beta, \quad (9)$$

where $\Phi(k_x, \omega, m_x, n_x, \alpha, \beta)$ is the unknown function. Taking into account the fact that, up to the higher orders,

$$\frac{\partial}{\partial z}g(k_x - m_x - n_x, \omega-\alpha) \approx -i\frac{(\omega-\alpha)n(\omega-\alpha)}{c}\sqrt{1-\frac{(k_x-m_x-n_x)^2c^2}{(\omega-\alpha)^2n^2(\omega-\alpha)}}g,$$

$$\frac{\partial}{\partial z}g(m_x, \alpha-\beta) \tag{10}$$

$$\approx -i\frac{(\alpha-\beta)n(\alpha-\beta)}{c}\sqrt{1-\frac{m_x^2c^2}{(\alpha-\beta)^2n^2(\alpha-\beta)}}g,$$

$$\frac{\partial}{\partial z}g(n_x, \beta) \approx -i\frac{\beta n(\beta)}{c}\sqrt{1-\frac{n_x^2c^2}{\beta^2n^2(\beta)}}g,$$

one can obtain from Eq. (8) with regard to Eq. (9) that

$$\Phi = i\frac{\omega^2}{4\pi^3c^3}\varphi,$$

where

$$\varphi(k_x, \omega, m_x, n_x, \alpha, \beta)$$

$$= \left(\omega n(\omega)\sqrt{1-\frac{k_x^2c^2}{\omega^2n^2(\omega)}}\right.$$

$$+ (\omega-\alpha)n(\omega-\alpha)\sqrt{1-\frac{(k_x-m_x-n_x)^2c^2}{(\omega-\alpha)^2n^2(\omega-\alpha)}} \tag{11}$$

$$+ (\alpha-\beta)n(\alpha-\beta)\sqrt{1-\frac{m_x^2c^2}{(\alpha-\beta)^2n^2(\alpha-\beta)}}$$

$$\left.+ \beta n(\beta)\sqrt{1-\frac{n_x^2c^2}{\beta^2n^2(\beta)}}\right)^{-1}.$$

Thus, the truncated nonlinear equation describing the nonparaxial dynamics of the spatial spectrum of unidirectional radiation takes the form

$$\frac{\partial g}{\partial z} + i\frac{\omega n(\omega)}{c}\sqrt{1-\frac{k_x^2c^2}{\omega^2n^2(\omega)}}g + i\frac{\chi\omega^2}{4\pi^3c}$$

$$\times\int\int\int_{-\infty}^{+\infty}\int\varphi(k_x, \omega, m_x, n_x, \alpha, \beta) \tag{12}$$

$$\times g(k_x-m_x-n_x, \omega-\alpha)$$

$$\times g(m_x, \alpha-\beta)g(n_x, \beta)dm_xdn_xd\alpha d\beta = 0,$$

where $\varphi$ is described by Eq. (11).

With regard to Eqs. (8)–(11), Eq. (12) after the procedure specified by Eq. (7) reduces to total Eq. (3) up to terms of the fifth order in $g$ [because of approximation (10)]. This accuracy is sufficient, because original spectral Eqs. (2) and (3) were derived from Eq. (1) with the same accuracy.

Equation (12) allows the analysis of the nonlinear evolution of light radiation, whose time and spatial spectra can both be very wide. The superbroadening of the time spectrum can be described correctly, because Eq. (12) takes into account an arbitrary dispersion of the linear refractive index of the medium, whereas there is no considerable dispersion of the nonresonant nonlinearity of the electron origin in a substantial part of the transparency range of dielectric materials [11]. The broadening of the spatial spectrum of radiation (e.g., due to self-focusing) can be described by Eq. (12) up to the spectrum width commensurable with the wavenumber. If the spatial spectrum involves frequencies $k_x$ exceeding the wavenumber, the second term in Eq. (12) is real. These spatial-spectrum components correspond to the fields that vary exponentially along $z$ and are similar to the fields arising at total internal reflection. The propagation of radiation with such a superbroadened spatial spectrum must be analyzed with allowance made for the possibility of generating the inverse wave [9, 12].

Let us approximately solve Eq. (12) describing the nonparaxial dynamics of the spectrum. Using the ansatz

$$g = U(z, k_x, \omega)\exp\left(-i\frac{\omega n(\omega)}{c}\sqrt{1-\frac{k_x^2c^2}{\omega^2n^2(\omega)}}z\right) \tag{13}$$

and applying the Pickard method of successive approximations [13], one can easily obtain the following solution of Eq. (12) in the first iteration:

$$U(z, k_z, \omega) = U_0(k_z, \omega)$$

$$+ \frac{\chi\omega^2}{4\pi^3}\int\int\int_{-\infty}^{+\infty}\int U_0(k_x-m_x-n_x, \omega-\alpha)$$

$$\times U_0(m_x, \alpha-\beta)U_0(n_x, \beta) \tag{14}$$

$$\times\left\{\exp\left[-i\frac{z}{c}\left(\varphi-\omega n(\omega)\sqrt{1-\frac{k_x^2c^2}{\omega^2n^2(\omega)}}\right)\right]-1\right\}$$

$$\times\varphi^{-1}\left[\varphi-\omega n(\omega)\sqrt{1-\frac{k_x^2c^2}{\omega^2n^2(\omega)}}\right]^{-1}dm_xdn_xd\alpha_xd\beta_x,$$

where $U_0(k_x, \omega)$ is the space–time spectrum of radiation at the entrance to the nonlinear medium (at $z = 0$).

The figure illustrates the application of solution (14) to simulate the nonlinear propagation of a pulse of a titanium–sapphire laser through quartz glass. The input space–time distribution of an extremely short pulse is taken as Gaussian

$$E(x, t) = E_0e^{-(x/\sigma)^2}e^{-(t/\tau)^2}\cos(\omega_0t),$$

and the dispersion of quartz glass is specified as

$$n(\omega) = N_0 + ac\omega^2. \tag{15}$$

Here, $N_0 = 1.45$; $ac\omega_0^2 = 0.007$; $\omega_0 = 2.4\times10^{15}$ s$^{-1}$; $\tau/T_0 = 3$, $\sigma/\lambda_0 = 3$, where $T_0 = 2\pi/\omega_0$ and $\lambda_0 = 2\pi c/\omega_0$;

and $3\pi\chi E_0^2/2n(\omega_0) = 0.0001$ has the meaning of a nonlinear addition to the refractive index (for the nonlinear refractive index of quartz glass $n_2 = 2.9 \times 10^{-16}$ cm$^2$/W, this addition arises at peak intensity $I = 0.5 \times 10^{12}$ W/cm$^2$).

Although solution (14) is obtained for the spectrum amplitude $U$, the figure illustrates the corresponding solution for the field $E$. Dynamic equation (12) and its approximation solution specified by Eqs. (13) and (14) can obviously be rewritten for the field $E$. However, their form for $E$ is more unwieldy than Eqs. (12)–(14). In particular, linearized Eq. (12) for the spectrum has the solution in the form of trivial algebraic relation (14), where $U = U_0$, whereas the dynamics of the field in a linear medium is described by the integral of the Airy function [14] even for simple dispersion dependence (15).

The figure shows an axonometric mapping of the variation of the transverse distribution of the normalized field $E/E_0$ and its time dynamics as the distance passed in the glass increases. Since the negative-field part of the extremely short pulse conserves the symmetry of the positive-field part of this pulse, the figure shows only the latter part (the negative-field part is below the $E = 0$ plane and is not seen in figure). In addition, the figure shows the plane images of the space–time field distribution (light and dark gray strips correspond to positive and negative field values, respectively). It is more difficult to estimate the absolute values of the field $E$ from these images, but changes in the radiation phase are more pronounced.

The figure indicates that the dispersion–diffraction smearing of the extremely short pulse due to medium nonlinearity is accompanied by the broadening of its spectrum. The high-frequency components are efficiently generated and separated from the "maternal" pulse due to dispersion. The extremely short pulse undergoes self-division. The classical third-harmonic generation is an analog of this effect for the quasi-monochromatic pulses. However, the spectrum of the harmonics, as well as the spectrum of the maternal extremely short pulse, is superbroadened in the case of the extremely short pulse. For this reason, it is impossible to analyze the interaction of continuum-spectrum components by the usual method of the slowly varying envelope, which is based on the approximation of quasi-monochromatic radiation. The formation of dumb-bell shaped light structures with various spectral compositions was observed in [8] in the process of self-focusing of an extremely short pulse. However, this effect was not treated as the self-division of the extremely short pulse. Moreover, it was considered in [8] on the verge of applicability of the paraxial approximation, which was basic in that work.

In summary, the nonparaxial dynamics of light pulses consisting of several light-field oscillations in nonlinear media with dispersion has been examined. It has been shown that the spectral approach to the analysis of the self-action of radiation with wide spatial and time spectra is more fruitful than the field approach. It has been demonstrated that the broadening of the spectrum of an extremely short pulse in a nonlinear medium can result in the self-division of the pulse.

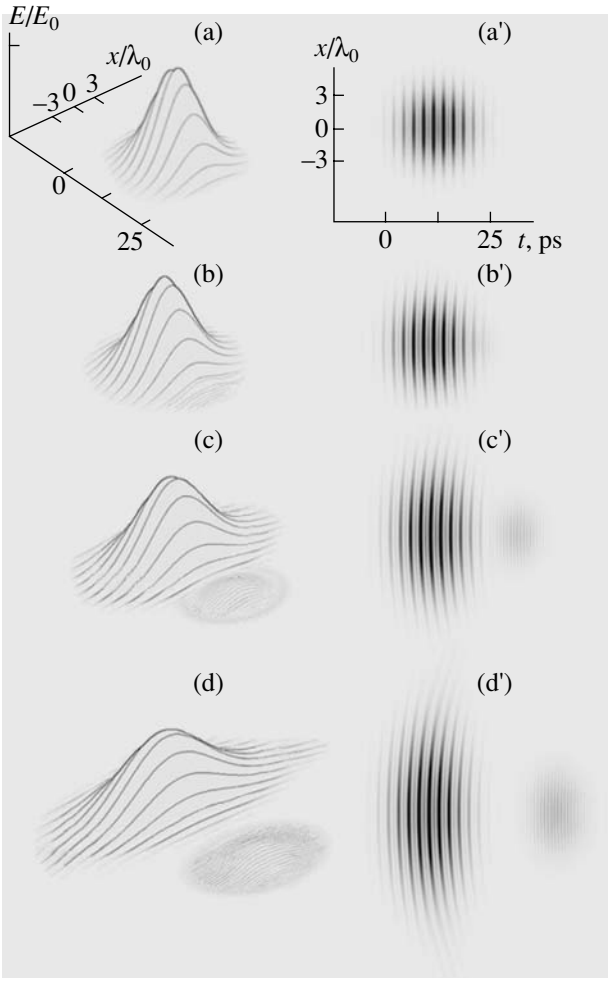


Spatial–time dynamics of the electric field of the extremely short pulse from a titanium–sapphire laser in quartz glass $z$ = (a, a') $0\lambda_0$, (b, b') $25\lambda_0$, (c, c') $50\lambda_0$, and (d, d') $75\lambda_0$.

The authors are grateful to A.N. Berkovskiĭ and Yu.A. Shpolyanskiĭ for stimulating discussion and recommendations concerning the procedure of illustrating solution (14).

This work was supported by the U.S. Civilian Research and Development Foundation for the Independent States of the Former Soviet Union (grant no. RP-2249), by the Russian Foundation for Basic Research (project no. 01-02-17841), and by the Program for Basic Research in Natural Sciences, Ministry of Education of the Russian Federation (grant no. E00-3.2-290).

## REFERENCES


1. Th. Brabec and F. Krausz, Rev. Mod. Phys. **72**, 545 (2000).
2. S. A. Akhmanov, V. A. Vysloukh, and A. S. Chirkin, *The Optics of Femtosecond Pulses* (Nauka, Moscow, 1988).
3. G. Agrawal, *Nonlinear Fiber Optics* (Academic, San Diego, 1995; Mir, Moscow, 1996).
4. A. I. Maĭmistov, Kvantovaya Élektron. (Moscow) **30**, 287 (2000).
5. S. A. Kozlov, Vestn. Molodykh Uchenykh, Ser. Fiz. Nauki, No. 1, 7 (2000).
6. É. M. Belenov and A. V. Nazarkin, Pis'ma Zh. Éksp. Teor. Fiz. **53**, 188 (1991) [JETP Lett. **53**, 200 (1991)].
7. S. A. Kozlov and S. V. Sazonov, Zh. Éksp. Teor. Fiz. **111**, 404 (1997) [JETP **84**, 221 (1997)].
8. A. N. Berkovskiĭ, S. A. Kozlov, and Yu. A. Shpolyanskiĭ, Opt. Zh. **69** (3), 35 (2002) [J. Opt. Technol. **69**, 163 (2002)].
9. S. A. Iz'yurov and S. A. Kozlov, Pis'ma Zh. Éksp. Teor. Fiz. **71**, 666 (2000) [JETP Lett. **71**, 453 (2000)].
10. M. B. Vinogradova, O. V. Rudenko, and A. P. Sukhorukov, *Theory of Waves* (Nauka, Moscow, 1990).
11. A. N. Azarenkov, G. B. Al'tshuler, N. R. Belashenkov, and S. A. Kozlov, Kvantovaya Élektron. (Moscow) **20**, 733 (1993).
12. M. D. Feit and J. A. Fleck, J. Opt. Soc. Am. B **5**, 633 (1988).
13. G. A. Korn and T. M. Korn, *Mathematical Handbook for Scientists and Engineers* (McGraw-Hill, New York, 1968; Nauka, Moscow, 1977).
14. L. A. Vaĭnshteĭn and D. E. Vakman, *Frequency Separation in the Theory of Oscillations and Waves* (Nauka, Moscow, 1983).


*Translated by R. Tyapaev*

JETP Letters, Vol. 76, No. 4, 2002, pp. 211–214. From Pis'ma v Zhurnal Éksperimental'noĭ i Teoreticheskoĭ Fiziki, Vol. 76, No. 4, 2002, pp. 246–250.


# Frictional Shear Cracks¶

**E. A. Brener* and V. I. Marchenko****

** Institut für Festkörperforschung, Forschungszentrum Jülich, D-52425 Jülich, Germany*

*** Kapitza Institute for Physical Problems, Russian Academy of Sciences, Moscow, 117334 Russia*

Received July 10, 2002

We discuss crack propagation along the interface between two dissimilar materials. The crack edge separates two states of the interface, "stick" and "slip." In the slip region, we assume that the shear stress is proportional to the sliding velocity; i.e., the linear viscous friction law is valid. In this picture, the static friction appears as the tile Griffith threshold for crack propagation. We calculate the crack velocity as a function of the applied shear stress and find that the main dissipation comes from the macroscopic region and is mainly due to the friction at the interface. The relevance of our results to recent experiments, Baumberger *et al.*, Phys. Rev. Lett. **88**, 075509 (2002), is discussed. © *2002 MAIK "Nauka/Interperiodica".*

PACS numbers: 46.50.+a; 46.55.+d; 62.20.Mk

A few recent experimental observations [1, 2] of the frictional motion of sheared gels sliding along a glass surface indicate the existence of self-healing pulses and inhomogeneous modes of sliding [3]. A regime of periodic stick slip has been observed in a limited range of small shearing rates [2]. It bifurcates towards stationary sliding at some critical driving velocity. The slip pulses traverse the sample with a velocity much larger than the driving velocity but still much smaller than the speed of sound.

Slip pulses in gels seem to be very different from Schallamach waves and "brittle" pulses studied by Gerde and Marder [4], since no observable interface separation occurs. In this respect, they are more comparable with self-healing cracks suggested by Heaton [5] in the context of seismic events.

Recent investigations (see, for example, [6] and references therein) point towards an essential importance of the underlying friction law in the slip state. It has been proved that the simple Coulomb friction leads to the so-called "ill-posedness" of the linear stability problem while discussing small nonhomogeneous perturbations of the stress and strain fields in a sliding mode [6]. Moreover, Caroli [7] has shown that the existence of slow, periodic slip pulses is incompatible with the Coulomb friction law.

In this letter, we discuss crack propagation along the interface between two dissimilar materials. The crack edge separates two states of the interface, "stick" and "slip." We assume that the interface is flat with a strong adhesion contact. In principle, we could allow for small wavelength surface roughness, but in this case we consider length scales larger than the longest wavelength component. In the presence of roughness, the assumption of strong adhesion and full contact at the interface presumably is only reasonable for "soft" materials with a relatively small shear modulus. Gels are clearly materials of this sort.

In the slip region we assume a simple linear viscous friction law, namely, that the shear stress is proportional to the sliding velocity. This law, strongly motivated from the theoretical point of view, is usually not discussed in the literature, since it does not lead to the so-called static friction phenomenon observed experimentally. However, we will see that in our description, static friction appears in a natural way as the usual Griffith threshold for crack propagation. The important point is that, before the system goes into a sliding mode, the slip pulse should traverse the sample. This requires a finite shear stress, since the stick state of the interface is energetically more favorable.

With the linear viscous friction law, we find conditions for crack propagation and calculate the crack velocity as a function of the applied shear stress. We find that the main dissipation comes from a macroscopic region and is due to friction at the interface. This situation is very different from usual crack propagation, where the main dissipation is localized in the microscopic tip region.

We also briefly discuss frictional shear cracks inside homogeneous materials. The point here is that in mode II (and in mode III) cracks, there is no macroscopic opening. If two surfaces remain in contact, the standard boundary conditions, namely, vanishing of the normal and shear stresses at the crack surfaces, are not theoretically motivated. The relative sliding velocity of the two surfaces should lead to nonzero shear stresses. Finally, we discuss the relevance of our results to the experimental observations [2].

Consider an elastic solid sliding on a flat rigid substrate. Assume that the elastic solid occupies the space $H > y > 0$, and let $(x, y, z)$ be a coordinate system with

¶This article was submitted by the authors in English.

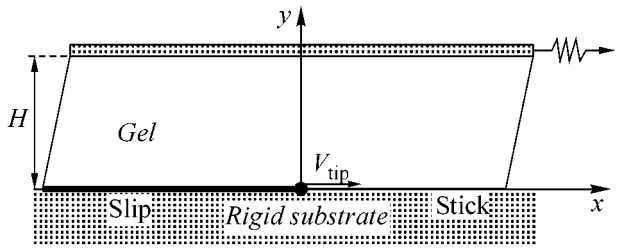


An elastic body sliding on a rigid substrate.

the plane $y = 0$ corresponding to the surface of the solid (see the figure). We discuss the plane strain situation with $u_z = 0$, where $u$ is the displacement vector. We assume that the interface can be in two states: "stick" and "slip." The boundary between these two states is described by the crack edge, which moves with a velocity $V_{tip}$ in the $x$ direction. In the stick region, the displacements are continuous, and, since we assume a rigid substrate, the boundary conditions are $u_x = u_y = 0$ for $x - V_{tip}t > 0$ and $y = 0$. In the slip region, we assume that the two solids (for all times) are in contact, $u_y = 0$ for $x - V_{tip}t < 0$ and $y = 0$, while we allow for a finite relative sliding velocity $\dot{u}_x$. This sliding velocity leads to a frictional shear stress at the interface, where we assume a linear viscous friction law

$$\sigma_{xy} = \alpha \dot{u}_x, \tag{1}$$

with $\alpha$ being the viscous friction coefficient. It is reasonable to assume that the interface energy in the stick phase is smaller than the interface energy in the slip phase, since the adhesion contact in the stick region is stronger. Let us denote this energy difference by $\gamma$. It is clear that without external loading, the stick phase is energetically favorable, and a finite shear stress is required to get the interface into the slip state. Let us assume that far ahead of the crack tip, the solid is homogeneously strained with $u^{\infty}_{xy}$ and stressed with $\sigma_{xy} = 2\mu u^{\infty}_{xy}$, where $\mu$ is the shear modulus. The strain energy is $\mu(u^{\infty}_{xy})^2 H$. Far behind the crack tip, where the stress is relaxed, only the interface energy $\gamma$ remains. The slip state will be realized only if $\Delta = \mu(u^{\infty}_{xy})^2 H/\gamma > 1$. In this case, the crack should propagate in the positive direction of $x$. Otherwise, the crack would propagate with a negative velocity, and the stick phase will be restored. Condition $\Delta = 1$ is nothing but the usual Griffith threshold for crack propagation. On the other hand, in the context of the friction problem, this condition may be interpreted as a static friction threshold: a finite shear loading is required to get the system into the sliding mode.

If the whole interface is in the slip state, steady-state motion of the elastic body is possible with a velocity

$$V = 2Su_{xy}, \tag{2}$$

where $S = \mu/\alpha$ is the velocity scale given by the friction law. We note that this homogeneous sliding mode is linearly stable for any velocity with respect to small nonhomogeneous perturbations of the stress and strain fields localized in the surface region. In this respect, the viscous friction law is very different from the Coulomb friction, which leads to a linear instability and ill-posedness of the problem as it has been intensively discussed in the literature [6].

On the other hand, the homogeneous sliding mode may be unstable against the resticking pulse (nonlinear "healing instability") if the corresponding value of $\Delta < 1$. Since, in this case, the strain, which defines the value of $\Delta$ is related to the steady-state sliding velocity by Eq. (2), we find that the homogeneous sliding is stable against the healing instability only above the critical sliding velocity

$$V_c = 2S(\gamma/\mu H)^{1/2}. \tag{3}$$

Now let us turn to the calculation of the crack tip velocity $V_{tip}$ as a function of the dimensionless driving force $\Delta$. The strategy is as follows: we solve the elastic problem in the vicinity of the crack tip and then calculate the energy flux into the crack tip and the dissipation due to the friction at the interface. Finally, using the energy balance, we find the crack velocity.

Let us start from some qualitative estimates. Assume that, as in the usual crack problem, the singular behavior of the displacement vector is given by a square-root singularity in the vicinity of the crack tip. Then the dissipation rate at the interface

$$J_d = \alpha \int (\dot{u}_x)^2 dx \tag{4}$$

depends logarithmically ($\sim \ln H/a$) on $H$. Thus, the main dissipation comes from the macroscopic region. In the usual crack problem, the main dissipation comes from the close vicinity of the tip and often requires the introduction of microscopic models. Here we have the chance to avoid such a detailed microscopic description by using some microscopic length scale $a$ as a cutoff, which enters only the logarithm in the final result. In this small region the used equations break down and an effective tip dissipation should be introduced. Due to bulk viscosity, there is an additional contribution $\eta \dot{u}_{ik}$ to the stress tensor. The dissipation rate diverges strongly at small distances (as $1/r$) and correspondingly decays at macroscopic distances. Thus, this effect can also be incorporated into the tip dissipation.

Now we solve the elastic problem more accurately, while still using a quasistatic approximation for the moment. The generalization to the full elastodynamic description is straightforward and will be given below.

In the co-moving frame of reference and in the vicinity of the crack tip, the displacement field for the static elasticity and the boundary conditions formulated above is

$$u_x = A\mathrm{Re}[yz^{\lambda-1} - i(3-4\nu)z^{\lambda}/\lambda], \qquad u_y = A\mathrm{Re}[iyz^{\lambda-1}]. \tag{5}$$

Here, $z$ is a complex coordinate $z = x + iy$, $\nu$ is the Poisson ratio, and $A$ is a real amplitude. The spectrum of $\lambda$ is purely real and given by the following equation:

$$\exp(i2\pi\lambda) = -\frac{1 + i\pi\varepsilon/2}{1 - i\pi\varepsilon/2}, \tag{6}$$

with

$$\varepsilon = \frac{1}{2\pi}\frac{3-4\nu}{1-\nu}\frac{V_{\mathrm{tip}}}{S}. \tag{7}$$

In the limit of small values of $|\varepsilon|$ for the leading crack displacement component, we have $2\lambda \approx 1 + \varepsilon$.

Having defined the displacement field, we can calculate the energy flux $J_i = \sigma_{ik}\dot{u}_k$ and the local energy release into a small semicircular region with some microscopic radius a around the crack tip,

$$J_0 = 2\pi\mu(3-4\nu)(1-\nu)V_{\mathrm{tip}}A^2a^{\varepsilon}. \tag{8}$$

The dissipation rate due to the interface friction with exclusion of the small region of size a close to the tip is given by Eq. (4):

$$J_d = \alpha(3-4\nu)^2A^2V_{\mathrm{tip}}^2\varepsilon^{-1}(\tilde{H}^{\varepsilon} - a^{\varepsilon}) = J_0[(\tilde{H}/a)^{\varepsilon} - 1]. \tag{9}$$

Here, $\tilde{H} = f(\nu)H$, with $f$ being an undetermined yet function of the Poisson ratio; $H$ is a thickness of the sample. This function can be found by solving the elastic problem for given geometry and all boundary conditions. As we will see the tip velocity does not crucially depends on the actual value of the factor $f$, which is of the order of unity.

On the other hand the local energy release into the crack tip $J_0$ must compensate the surface energy difference: $J_0 = \gamma V_{\mathrm{tip}}$. Note that here we have neglected the dissipation at the tip in comparison with the energy release $\gamma V_{\mathrm{tip}}$, which is reasonable at small tip velocities compared to the velocity of sound. Finally, using the global energy conservation law,

$$J_\infty = J_0 + J_d = \mu(u_{xy}^{\infty})NV_{\mathrm{tip}}, \tag{10}$$

we find

$$\varepsilon = \frac{\ln\Delta}{\ln(\tilde{H}/a)} \approx \frac{\ln\Delta}{\ln(H/a)}. \tag{11}$$

Since $\varepsilon$ is given by Eq. (7), this result is a compact representation of the crack velocity as a function of the driving force $\Delta = \mu(u_{xy}^{\infty})H/\gamma$. Note that $\Delta = 1$ corresponds to Griffith equilibrium. Equation (11) is valid for small $|\varepsilon|$. The explicit expression for the crack velocity reads

$$V_{\mathrm{tip}} = 2\pi\frac{1-\nu}{3-4\nu}\frac{\ln\Delta}{\ln(H/a)}S. \tag{12}$$

In the case of small $\Delta - 1$, we obtain

$$V_{\mathrm{tip}} \approx 2\pi\frac{1-\nu}{3-4\nu}\frac{\Delta-1}{\ln(H/a)}S. \tag{13}$$

This result corresponds to a small dissipation rate compared to the total energy flux, $J_d \ll J_\infty$, and can also be obtained using perturbation theory: we solve the elastic problem neglecting friction ($\sigma_{xy} = 0$ at the interface) and then calculate the dissipation rate (4) using this solution as zero order displacement field.

Up to now, we have used the static approximation. The tip velocity should be small compared to the sound velocity. The elastodynamic generalization is straightforward. Using the standard approach to the singular solutions near the crack tip [8], we find the displacement field $u$

$$u_x = A\mathrm{Re}\left[\frac{(x + i\alpha_d y)^{\lambda}}{i\alpha_d} + i\alpha_s(x + i\alpha_s y)^{\lambda}\right], \qquad u_y = A\mathrm{Re}[(x + i\alpha_d y)^{\lambda} - (x + i\alpha_s y)^{\lambda}] \tag{14}$$

with $\alpha_d^2 = 1 - (V_{\mathrm{tip}}/C_d)^2$ and $\alpha_s^2 = 1 - (V_{\mathrm{tip}}/C_s)^2$, where $C_d$ and $C_s$ are dilation and shear wave speed. The spectrum of $\lambda$ is still given by Eq. (6) but now $\varepsilon$ reads

$$\varepsilon = \frac{2}{\pi}\frac{(1 - \alpha_d\alpha_s)}{\alpha_d(1 - \alpha_s^2)}\frac{V_{\mathrm{tip}}}{S}. \tag{15}$$

Thus, elastodynamic effects lead to a redefinition of $\varepsilon$ in the main result, Eq. (11), which remains valid. For small velocities, Eqs. (14) and (15) reduce to Eqs. (5) and (7), respectively.

The most serious problem with large velocities arises in connection with a self-consistent description of the dissipation at the tip. This part of kinetics cannot be considered macroscopically for arbitrary tip velocities. One can only treat the case of small velocities, $V_{\mathrm{tip}} \ll C_s$ in a model independent way, by introducing the tip kinetic coefficient. For higher velocities the so-called velocity dependent fracture energy $\gamma(V_{\mathrm{tip}})$ is introduced. This function contains information about the usual surface energy $\gamma$ and tip dissipation and reduces to the surface energy in the static limit. The main dissipation in our approach arises from the friction between both sides of the crack and can be treated macroscopically. Note that this part of the dissipation can be described by the velocity independent friction coefficient $\alpha$ even at large tip velocities in the case of small sliding velocities.

Up to now, we have discussed shear cracks along the interface between two dissimilar materials (the case of a rigid substrate). We also present the result for the case of frictional shear cracks inside homogeneous elastic materials. Such cracks can propagate under the shear loading in amorphous materials, or along grain boundaries in crystals (in single crystals the well known dislocation mechanism of plasticity should be favorable). The boundary conditions on the crack surfaces, which remain in contact, are the following: continuous normal displacement and continuous normal and shear stresses. The shear stress is also given by Eq. (1) with $\dot{u}_x$ being the relative sliding velocity of two crack surfaces. We note that these boundary conditions are quite different from the standard boundary conditions of mode II (and III) cracks: zero normal and shear stresses on the crack surfaces [8]. In our case, for the frictional shear crack, we find the following expression for $\varepsilon$ which enters the general result, Eq. (11):

$$\varepsilon = \frac{4}{\pi}\frac{\alpha_s(1-\alpha_s^2)}{4\alpha_d\alpha_s - (1+\alpha_s^2)}\frac{V_{\text{tip}}}{S}. \qquad (16)$$

Now let us discuss the relation of our results to experimental observations of Baumberger, Caroli, and Ronsin [2]. They performed experiments of a gel sliding on a glass plate. The driving velocity was given and the shear force and thus the average shear stress was deduced from the spring elongation. Above some critical driving velocity $V_c \approx 125$ μm/s, steady sliding was observed. At velocities smaller than the critical one, periodic stick slip sets up (see figures in [2]). Upon increasing the driving velocity $V$, no hysteresis of the transition was detected. In the stick slip regime, they observed the propagation of self-healing pulses with no opening, nucleated periodically at the trailing edge of the sample. The propagation velocity of these cracks was about 60 times larger than the critical sliding velocity, yet still much smaller than the shear wave speed.

The existence of a critical sliding velocity, where stationary sliding is stable against the healing instability, appears naturally in our description and is given by Eq. (3). The characteristic value of the shear strain in the sliding mode near the critical velocity experimentally was about $u_{xy} = 0.04$. Thus, we can estimate from Eq. (2) the characteristic velocity $S = 1.5$ mm/s, and from Eq. (3), we find that the characteristic difference between the interface energies in the slip and stick states is $\gamma = 0.1$ J/m$^2$. One would expect that for ordinary elastic materials, the velocity $S$ should be of the order of the speed of sound. However, for gels the shear modulus $\mu$ is much smaller than for ordinary materials. The shear wave speed $C_s = (\mu/\rho)^{1/2}$ is only 2 m/s. The velocity $S = \mu/\alpha$ is linear in $\mu$ and should be even smaller. This is a possible explanation for a relatively small value of $S$ compared to $C_s$.

In the stick-slip regime, which exists below $V_c$, the nucleation of a slip pulse takes place at the trailing edge of the sample and requires overshooting above the Griffith threshold according to the experiment. This overshooting is not small, and in order to estimate the crack velocity, we can use Eq. (12) since the velocity is still much smaller than the speed of sound. Because of the week logarithmic parameter dependence, we conclude that $V_{\text{tip}}$ is of the order of $S$ and essentially independent of the driving velocity in agreement with experimental observations. After the slip pulse traversed the sample, the stress drops below the Griffith threshold and, resticking takes place via propagation of a healing pulse. Its velocity is still described by Eq. (12) with $\Delta < 1$. This periodic stick slip regime bifurcates towards stationary sliding at $V = V_c$, where stresses are always above the Griffith threshold. For driving velocities slightly below $V_c$, characteristic values of $\Delta$ for resticking are close to 1. Since the velocity of the resticking crack is small and comparable with the driving velocity in this range, a complicated collective behavior of self-healing pulses is observed [2].

While our results are in qualitative agreement with experimental observations, we still underestimate the crack velocity, which is a few times smaller than in the experiment. On the other hand, the geometry of the experiment is such that the total macroscopic friction of the sliding sample obviously depends on the processes taking place at the edges of the sample. The stresses here are highly inhomogeneous, and the kinetic phenomena should be considered with a great care.

The observed nonlinear behavior of the stress with the velocity for relatively high sliding rates (the so-called shear-thinning rheology) can be in principle incorporated into a more sophisticated version of theory presented here. Another subject of future investigations should be the collective behavior of self-healing pulses in the spirit of [7]. Further theoretical and experimental investigations are needed to shed light on this phenomenon, where two intriguing problems, crack propagation and friction, come together.

Discussions with S.V. Iordauskii, B.N.J. Persson, and D.E.Temkin are greatly appreciated. V.M. thanks Forschungszentrum Jülich for its hospitality.

## REFERENCES

1. M. Rubio and J. Galeano, Phys. Rev. E **50**, 1000 (1994).
2. T. Baumberger, C. Caroli, and O. Ronsin, Phys. Rev. Lett. **88**, 075509 (2002).
3. B. N. J. Persson, *Sliding Friction: Physical Principles and Applications* (Springer-Verlag, Heidelberg, 2000).
4. E. Gerde and M. Marder, Nature (London) **413**, 285 (2001).
5. T. Heaton, Phys. Earth Planet. Inter. **64**, 1 (1990).
6. K. Ranjith and J. Rice, J. Mech. Phys. Solids **49**, 341 (2001).
7. C. Caroli, Phys. Rev. E **62**, 1729 (2000).
8. L. B. Freund, *Dynamic Fracture Mechanics* (Cambridge Univ. Press, New York, 1990).

*JETP Letters, Vol. 76, No. 4, 2002, pp. 215–217. Translated from Pis'ma v Zhurnal Éksperimental'noĭ i Teoreticheskoĭ Fiziki, Vol. 76, No. 4, 2002, pp. 251–253.*


# Transformation of the Magnetic Structure of $FeBO_3$ under High Pressures

**V. P. Glazkov[1], S. E. Kichanov[2,] *, D. P. Kozlenko[2], B. N. Savenko[2], and V. A. Somenkov[1]**

[1]*Russian Research Centre Kurchatov Institute, pl. Kurchatova 1, Moscow, 123182 Russia*

[2]*Joint Institute for Nuclear Research, Dubna, Moscow region, 141980 Russia*

* *e-mail: ekich@nf.jinr.ru*

Received July 5, 2002

The transformation of magnetic structure under hydrostatic and quasi-hydrostatic pressures up to 4 GPa was studied for iron borate $FeBO_3$ by the neutron diffraction method. Under quasi-hydrostatic conditions, the orientation of iron magnetic moments changes at pressures $P \geq 1.4$ GPa. Under hydrostatic conditions, no changes in the magnetic structure of iron borate were observed up to 2.1 GPa. This behavior is caused by the influence of the inhomogeneity (in magnitude and direction) of elastic stresses on the configuration of magnetic sublattices. © *2002 MAIK "Nauka/Interperiodica".*

PACS numbers: 75.80.+q; 62.50.+p; 61.12.Ld; 75.30.Kz

Structural and magnetic studies of iron borate $FeBO_3$ are of interest because of the magnetic phase transitions occurring in it with a change in temperature and pressure [1–8]. Under normal conditions, $FeBO_3$ has rhombohedral structure, in which the magnetic moments of iron ions are oriented perpendicular to the crystallographic axis (111) and are nearly antiparallel. The angle between them is $\beta \sim 0.9°$, so that the resulting weak ferromagnetic moment lies in the basal plane [2].

Interest in rhombohedral antiferromagnets has been renewed because of the methodological advances in high-pressure solid-state studies with the use of neutron and synchrotron radiation.

Earlier, the pressure-induced transformations of the magnetic structure of iron borate were studied by neutron diffraction in [3, 4]. It was established that, as was predicted in [5], the spin-orientational phase transition resulting in a change in the angle $\varphi$ between the magnetic moments of Fe ions and the crystallographic axis (111) occurs at $P \sim 1.7$ GPa. However, in more recent hydrostatic synchrotron-radiation and Mössbauer studies of $FeBO_3$ single crystals, this phase transition was not observed. At higher pressures ($P \sim 44$ GPa) and room temperature, the transition from the antiferromagnetic state to the nonmagnetic state was observed in $FeBO_3$ [6], and, on further increase in pressure (up to $P \sim 53$ GPa), the isostructural phase transition was observed, which was accompanied by the abrupt change in the volume of unit cell [7]. Therefore, the neutron and Mössbauer data have come into conflict with each other. It is the purpose of this work to reveal the possible reasons for this contradiction.

According to [8], the inhomogeneity of internal stresses may strongly affect the spin-reorientational phase transition in weak ferromagnets. This fact has motivated us to study the influence of high pressure on the magnetic structure of $FeBO_3$ under the hydrostatic and quasi-hydrostatic experimental conditions.

Experiments were performed with a DN-12 spectrometer on the pulsed high-flow IBR-2 reactor at the Joint Institute for Nuclear Research (Dubna). Polycrystalline $FeBO_3$ samples with a volume of 2.5 $mm^3$ were placed in a high-pressure cell with sapphire anvils [9]. The hydrostatic pressure was produced using special "Fluorinert" fluid. Under quasi-hydrostatic conditions (without the transmitting medium), experiments were conducted below 4 GPa, and under hydrostatic conditions, below 2.1 GPa, above which Fluorinert crystallized, and hence, the hydrostatic conditions were broken in part. The pressure in the chamber was determined from the shift of the ruby luminescence line with an accuracy of better than 0.05 GPa. The measuring time for one spectrum was 20 h on the average. The experimental data were processed using the "MRIA" [10] and "Fullproof" [11] programs based on the standard Rietveld method [12]. While processing the diffraction spectra, the parameters of hexagonal rhombohedral unit cell (*a* and *c* axes), the positional parameter *x* of oxygen atoms, the iron magnetic moment *M*, and the angle $\varphi$ between the crystallographic axis (111) and the vectors of iron magnetic moments were refined. Refinement was made using the standard models (space group $R\bar{3}c$) [1, 2].

One can see from the diffraction spectra of $FeBO_3$ presented in Fig. 1 that the intensity of magnetic peak (111) decreases with increasing pressure, while the intensity of magnetic peak (100) virtually does not change. This fact indicates that the orientation of iron

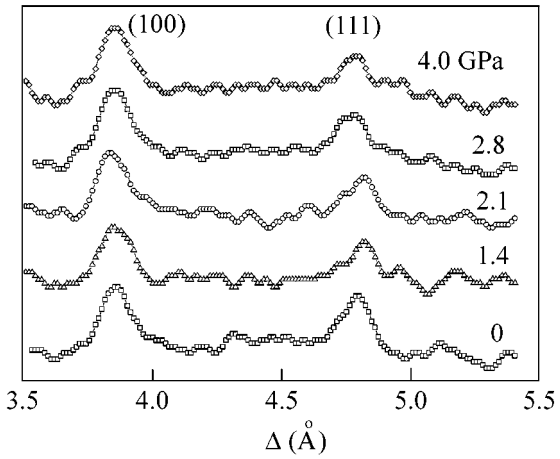


**Fig. 1.** Portions of diffraction spectra of $FeBO_3$ measured at 0, 1.4, 2.0, 2.8, and 4.0 GPa and normalized to the effective neutron flux. Scattering angle $2\theta = 45.5°$.

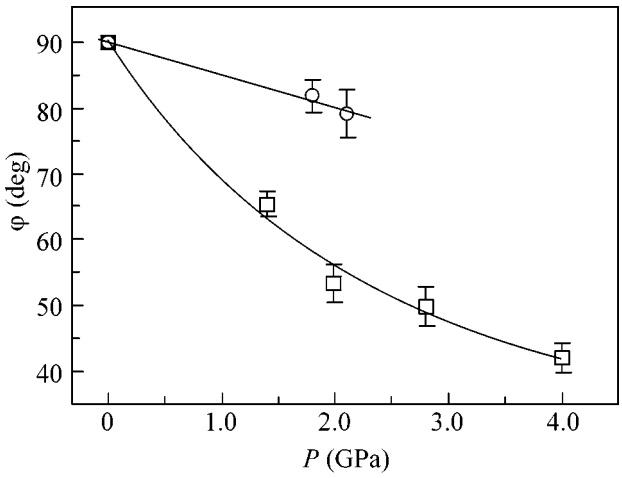


**Fig. 2.** Pressure dependence of the angle φ between the iron magnetic moments and the crystallographic axis (111).

magnetic moments about the crystallographic axis (111) changes. In principle, the explanation based on a two-phase model of $FeBO_3$ borate under pressure should not be ruled out. With the buildup of pressure, the volume with weak ferromagnetism in the sample decreases, while the volume of a purely antiferromagnetic phase increases. A change in the intensity of magnetic peak (111) under hydrostatic pressure is appreciably smaller.

The pressure dependence of angle φ between the magnetic moment and the crystallographic axis (111) is shown in Fig. 2. Under hydrostatic pressure, the angle φ changes only slightly, whereas it decreases from 90° to 42° upon the buildup of pressure to 4.0 GPa. The pressure dependence of the hexagonal parameters *a* and *c* is shown in Fig. 3. With an increase in pressure, the ratio *c*/*a* decreases from 3.123(5) to 3.110(5).

The magnetic structure of iron borate consists of two magnetic sublattices of Fe atoms with oppositely directed magnetic moments. According to [2], the thermodynamic potential for this system can be written as

$$\Phi = \Phi_m + \Phi_{ml} + \Phi_l + \Phi_{st}, \quad (1)$$

where $\Phi_{ml}$ is the energy of magnetoelastic interaction, $\Phi_l$ is the elastic energy, and $\Phi_{st}$ is the energy of external stresses.

In the presence of an applied external pressure, the expression for the energy of external stresses has the following form for a polycrystalline sample:

$$\Phi_{st} = P\sum_{(i)} U_{ii} + \sum_{(i,j)} \sigma_{ij} U_{ij}, \quad (2)$$

where $\sigma_{ij}$ are the stress tensor components and $U_{ij}$ is the strain tensor components.

It follows from Eq. (2) that the configuration of sublattice magnetic moments in a polycrystalline sample under quasi-hydrostatic pressure is a function not only of pressure *P* but also of the external elastic stresses $\sigma_{ik}$ [8]. Moreover, the stress-induced transformations may be quite significant because of the strengthening effect of exchange forces [5]. Therefore, the spin-orientational phase transition observed in [3, 4] can be treated as a change in the configuration of magnetic sublattices induced by external elastic stresses.

As for the single-crystal samples, it was predicted in [13] that the external pressure is "switched off" in rhombohedral antiferromagnets in the sense that, if the pressure is applied along the *z* axis (as in [6]), then the magnetic system does not "feel" the pressure, irrespective of its magnitude, while, for the pressure applied in

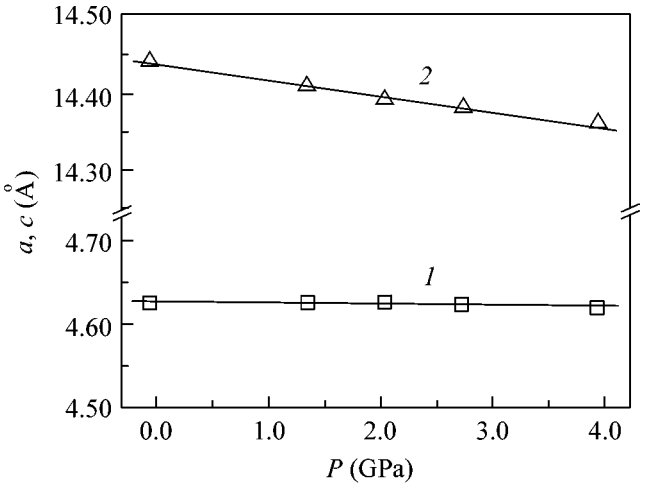


**Fig. 3.** Pressure dependence of the parameters (*1*) *a* and (*2*) *c* of the hexagonal unit cell. Solid lines are linear extrapolations of the experimental data. The errors of experimental bars do not exceed the symbol sizes.

the perpendicular direction (along the *y* axis), the spin-reorientational transition pressure is minimal (0.2 and 0.6 GPa for $Fe_2O_3$ and $FeBO_3$, respectively). Hence, the absence of the transition in the Mössbauer single-crystal experiments and its presence in the polycrystalline neutron experiments may be considered as the experimental confirmation of the effect predicted in [13]. As for the transitions at higher pressures (up to 50 GPa), for which the purely hydrostatic conditions cannot be produced in practice, the influence of elastic stresses on the configuration of magnetic sublattices may be appreciable. This may be the reason why the experimental (53 GPa) and theoretical (23 GPa) transition pressures differ for $FeBO_3$ under high pressures [14].

This work was supported by the Russian Foundation for Basic Research (project no. 00-02-17077) and the Ministry of Industry, Science, and Technologies of the Russian Federation (state contract no. 40.012.1.1.1148 and grant for the support of unique Russian plants).

## REFERENCES

1. R. Diehl, W. Jantz, B. I. Noland, *et al.*, Curr. Top. Mater. Sci. **11**, 241 (1984).
2. I. E. Dzialoshinskiĭ, Zh. Éksp. Teor. Fiz. **32**, 1547 (1957) [Sov. Phys. JETP **5**, 1259 (1957)].
3. V. P. Glazkov, V. V. Kvardakov, and V. A. Somenkov, Pis'ma Zh. Éksp. Teor. Fiz. **71**, 238 (2000) [JETP Lett. **71**, 165 (2000)].
4. V. P. Glazkov, V. V. Kvardakov, and V. A. Somenkov, High Press. Res. **17**, 6 (2000).
5. A. S. Pakhomov, Fiz. Met. Metalloved. **25**, 5 (1968).
6. I. A. Troyan, A. G. Gavrilyuk, V. A. Sarkisyan, *et al.*, Pis'ma Zh. Éksp. Teor. Fiz. **74**, 26 (2001) [JETP Lett. **74**, 24 (2001)].
7. A. G. Gavriliuk, I. A. Trojan, R. Boehler, *et al.*, Pis'ma Zh. Éksp. Teor. Fiz. **75**, 25 (2002) [JETP Lett. **75**, 23 (2002)].
8. P. P. Maksimenkov and V. I. Ozhogin, Zh. Éksp. Teor. Fiz. **65**, 657 (1973) [Sov. Phys. JETP **38**, 324 (1973)].
9. V. P. Glazkov and I. N. Goncharenko, Fiz. Tekh. Vys. Davleniĭ **1**, 181 (1991).
10. J. Rodrigues-Carvajal, Physica B (Amsterdam) **192**, 55 (1993).
11. V. B. Zlokazov, Comput. Phys. Commun. **85**, 415 (1995).
12. H. M. Rietveld, Appl. Crystallogr. **2**, 65 (1969).
13. V. I. Ozhogin and R. M. Farzetdinova, Preprint No. 3624, IAÉ (Ins. of Atomic Energy, Moscow, 1987).
14. K. Parlinski, Eur. Phys. J. B **27**, 283 (2002).

*Translated by V. Sakun*

JETP Letters, Vol. 76, No. 4, 2002, pp. 218–221. Translated from Pis'ma v Zhurnal Éksperimental'noĭ i Teoreticheskoĭ Fiziki, Vol. 76, No. 4, 2002, pp. 254–257.


# On the Nature of the Kaiser Effect in Metallic Glasses

**A. S. Bakai[1], S. A. Bakai[1,] *, I. M. Mikhaĭlovskii[1], I. M. Neklyudov[1], P. I. Stoev[1], and M.-P. Macht[2]**

[1]*Kharkov Institute of Physics and Technology, Ukrainian Scientific Center, ul. Akademicheskaya 1, Kharkov, 310108 Ukraine*

** e-mail: serg.bakai@kipt.kharkov.ua*

[2]*Hahn-Meitner-Institut Berlin, Germany*

Received April 11, 2002; in final form, July 10, 2002

The Kaiser effect was observed in the measurement of acoustic emission (AE) during the course of uniaxial compression of the bulk samples of metallic glasses $Zr_{41}Ti_{14}Cu_{12.5}Ni_{10}Be_{22.5}$ and $Zr_{52.5}Ti_5Cu_{17.9}Ni_{14.6}Be_{22.5}$. The field-ion microscopy study of bulk $Zr_{41}Ti_{14}Cu_{12.5}Ni_{10}Be_{22.5}$ shows that this glass has a polycluster structure. This fact allows one to reveal the nature of AE appearing during the course of deformation of metallic glasses and to interpret the observed Kaiser effect. The dislocations generated at the intercluster boundaries and moving through the glass bulk are the sources of AE. © *2002 MAIK "Nauka/Interperiodica".*

PACS numbers: 62.65.+k; 61.43.Fs

The Kaiser effect [1, 2] appears in the testing of samples in the repetitive loading and unloading regime and lies in the fact that the acoustic emission (AE) appears in every subsequent loading only from the instant of time when the stress exceeds its maximal value achieved in the preceding loading. In crystalline materials, the Kaiser effect is explained by the dislocation glide and pinning processes. As to metallic glasses, the Kaiser effect in these systems and its nature still remain to be understood.

The Kaiser effect (in the extension of strip samples with a thickness of 100 μm) in fast-quenched amorphous alloys was first mentioned in [3], although no data of measurements were reported there. The nature of this effect, as well as the nature of AE appearing before the formation of shear bands, remains to be clarified [4].

The assumptions about the structure of metallic glasses and the structural defects as sources of plastic strain are in many respects contradictory and controversial [5–11]. Today, the free-volume model, the dislocation–disclination model, and the polycluster model are the most popular structural models of metallic glasses. In the polycluster model, contrary to the other models, the diffusion and slip at the intercluster boundaries play the main role in the plastic deformation processes.

In the free-volume model [9–11], the AE-generating inelastic structural rearrangements occur in the vicinity of large interatomic voids or micropores. According to this model, an additional free volume may appear with increasing tensile stress, eventually giving rise to the shear bands and the crack extension accompanied by the AE generation. Qualitatively, these considerations could be used to interpret the AE appearing upon the strip tension. One can assume that these AE sources arise in the course of deformation because of the appearance of an additional free volume. However, the generation of free volume is suppressed in the case of uniaxial compression of bulk samples (this is practically impossible for thin strips), because a uniform compression component arises in this case.

To explain the plastic deformation processes in the free-volume model, one assumes that they are caused by the cooperative rearrangement of atomic groups in the local regions with a higher content of free volume. It is thought that the rearranged atomic groups are comparatively small (~10–20 atoms) [10] and uniformly distributed in glass. For this reason, no effective sources of ultrasonic radiation appear in this model, at least at the initial deformation stage prior to the formation of shear bands.

It was conjectured in [12] that the dislocationlike defects serve as AE source in metallic glasses, but the structure of these defects was not determined.

In [6, 5], a polycluster model of amorphous solids was proposed. Simultaneously, the theory of polycluster plastic deformation was developed, the structural defects (including dislocations) in glass were described, and the conditions were determined under which the defects can move at large (compared with the cluster size) distances.

According to the polycluster model, metallic glasses consist of noncrystalline clusters, i.e., of clusters whose atomic structure is translationally noninvariant (see [5]). In the low-temperature range (at temperatures lower than the vitrification temperature by 200 K), the slip at cluster boundaries and the dislocation motion through the clusters are the main mechanism of plastic

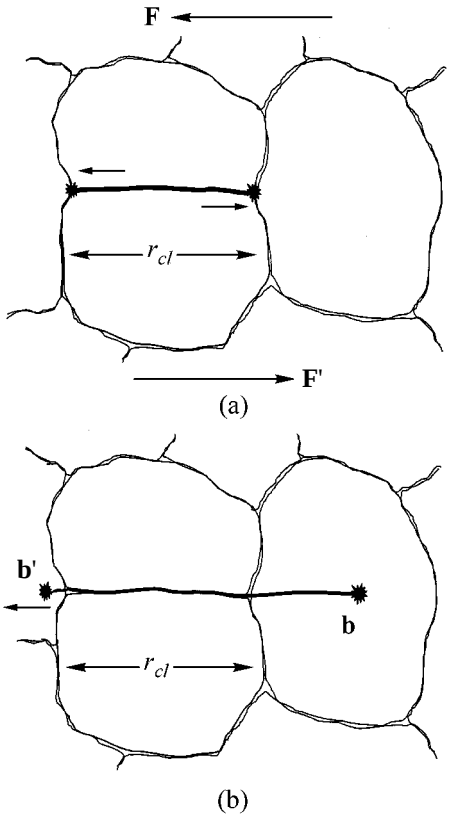


**Fig. 1.** Schematic representation of the slip at the intercluster boundary and the propagation of a dislocation generated at the intercluster boundary into the cluster. (a) Slip generated by the external forces **F** and **F**' at the intercluster boundary (shown by thick line) and blocked by the neighboring clusters at the triple joints. (b) Movement of the dislocation, generated at the intercluster boundary, into the cluster in the presence of shear stresses exceeding shear strength for the boundaries. The vectors **b** and **b**' indicate the orientation of Burgers vectors.

strain. These processes at their initial stages are schematically illustrated in Fig. 1.

The formation of bulk metallic glasses opens up new possibilities of studying this effect, because it allows the study of AE in bulk samples, in which one can achieve a higher total AE intensity upon compression.

The Kaiser effect appears because the AE-inducing inelastic rearrangement upon unloading is irreversible. The initial structural state is not regained, because the process has activation character and, hence, is suppressed at low temperature. Our investigations show that the Kaiser effect in the experiments with repetitive compression and unloading of bulk metallic glasses is observed prior to the formation of shear bands (see below). The slip processes, schematically illustrated in Fig. 1, are the most probable reason for this effect.

To check the validity of this statement, we studied the structures of metallic glass $Zr_{41}Ti_{14}Cu_{12.5}Ni_{10}Be_{22.5}$ by field-emission microscopy. Measurements were

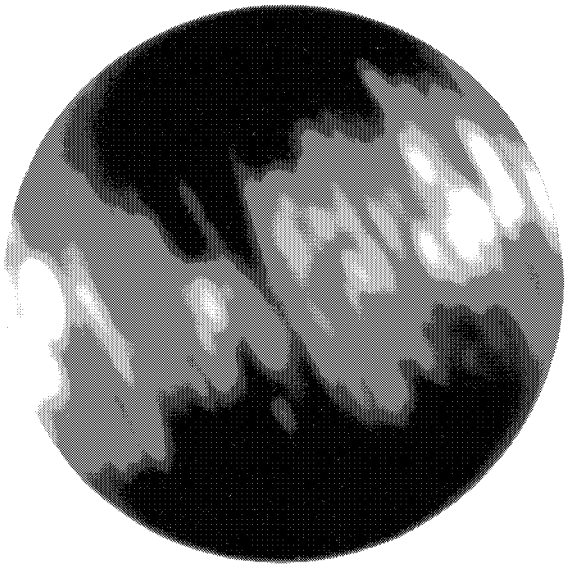

**Fig. 2.** Contrast bands of enhanced brightness in the field-ion microscopy image of bulk amorphous $Zr_{41}Ti_{14}Cu_{12.5}Ni_{10}Be_{22.5}$ alloy.

made in a two-chamber field-ion microscope with cooling to 53–78 K. Needlelike samples capped by elliptic paraboloids were prepared by electrochemical etching at a constant voltage of 5–15 V in a 10% solution of perchloric acid and ethyl alcohol. The minor and major radii of principal curvature at the apex of knifelike samples were in the range 3–10 and 50–500 nm, respectively. In the presence of intrinsic interfaces in the samples, saddlelike microgrooves were formed in the course of polishing the surface of nonaxisymmetrical points by low-temperature field evaporation, and, as a consequence, banded contrast appeared in the ion-microscopic images [13].

The ion-microscopic data showed that the field-emission images of knifelike samples with a thickness on the order of 10 nm were characterized by the presence of bright contrast bands that were retained in the course of field evaporation (Fig. 2). In the analysis of the banded contrast, the angular dependence of the local linear magnification was taken into account. In particular, the contrast bands along the normal to the foil plane in Fig. 2 dominated because the local magnifications in the principal cross-sectional planes of the apices of nonaxisymmetrical samples were different. The separation between the bands was within 5–15 nm. The thickness of the evaporated layer was estimated with an accuracy of 50% by measuring the working stress. Within this accuracy, it coincided with the average distance between the contrast bands. The thin-foil field-ion microscopic study of the banded contrast at the interfaces in the knifelike samples showed [14, 15] that the bands appear due to the developed network of internal two-dimensional interfaces in fast-quenched

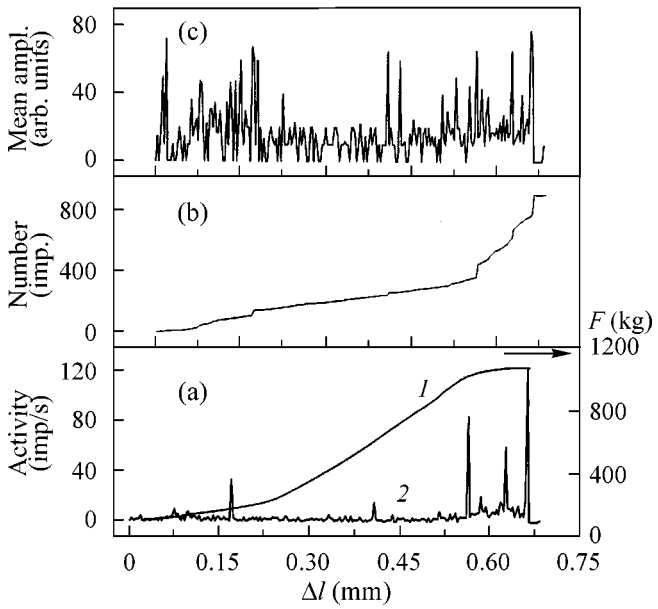


**Fig. 3.** Dependence of the AE parameters on the grip displacements ($\Delta l$) in the course of uniaxial compression of the bulk samples of metallic glass at room temperature. (a): (*1*) Loading and (*2*) AE activity. (b) Total number of pulses. (c) Mean amplitude of pulses.

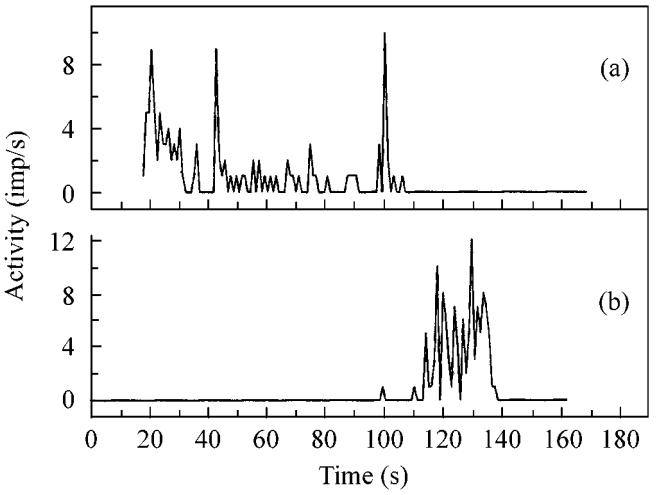


**Fig. 4.** Time dependences of pulse activity in the course of uniaxial compression. (a) First compression and (b) second compression.

amorphous alloys. The presence of bright contrast bands is due to the local variations of magnification in the vicinity of the outcrops of internal interfaces. An analysis of the banded contrast and its evolution during the process of field evaporation indicates that the bulk $Zr_{41}Ti_{14}Cu_{12.5}Ni_{10}Be_{22.5}$ alloy contains internal interfaces (intercluster boundaries) whose average density is on the order of $10^6$ cm$^{-1}$. The characteristic cluster sizes lie in the range 5–15 nm.

The AE was studied on equipment consisting of a universal testing machine 1958-U10 and a multichannel acoustic system M400. The AE gauge was fabricated from lead zirconate–titanate piezoelectric ceramics and had a resonance frequency of 180 kHz.

The samples were compressed with a rate of $10^{-3}$ s$^{-1}$ at room temperature. The acoustic parameters were measured in synchronism with the measurement of mechanical characteristics.

Experiments were performed using samples with diameter $d_0 = 3$ mm and height $h_0 = 4$ mm. The samples were cut from a 100-mm-long rod by the electric-spark method.

The results of measuring the AE upon uniaxial loading of a bulk sample of metallic glass $Zr_{52.5}Ti_5Cu_{17.9}Ni_{10}Al_{10}$ up to its damage are presented in Fig. 3, and the results for the repetitive loading below the damage threshold are presented in Fig. 4. The mechanical properties of this metallic glass were studied in [16] for various deformation regimes (various temperatures and deformation rates).

It is remarkable that, after unloading, no measurable plastic strain was observed in the sample; i.e., the microscopic plastic deformation processes did not generate macroscopic plastic strain in the sample. This signifies that the AE-generating sources are isolated and are small compared to the sample size. The slip arising at the intercluster boundaries and thereupon propagating into the clusters seems to be the natural AE source in the course of deformation of glass with structure shown in Fig. 2.

We also observed the recovery of the Kaiser effect; i.e., the AE was restored upon subsequent loading after the short-time (5–7 min) annealing of the sample at a temperature of ~670 K (30° lower than the vitrification temperature). The results of these measurements will be reported elsewhere.

Note in conclusion that our studies of the structure of bulk metallic glasses and the AE generated upon the low-temperature compression show that these glasses have the polycluster structure and that the slip at the intercluster boundaries and inside the clusters is the most probable AE source. Slip generates the Kaiser effect at low temperature, which prevents back relaxation.

## REFERENCES

1. V. A. Greshnikov and Yu. B. Drobot, *Acoustical Emission* (Izd. Standartov, Moscow, 1976).
2. V. A. Strizhalo, Yu. V. Dobrovol'skiĭ, and V. A. Strel'chenko, *Strength and Acoustical Emission of Materials and Structural Components* (Naukova Dumka, Kiev, 1990).

3. A. P. Braginskiĭ, A. Yu. Vinogradov, and A. M. Leksovskiĭ, Pis'ma Zh. Tekh. Fiz. **12**, 1111 (1986) [Sov. Tech. Phys. Lett. **12**, 459 (1986)].
4. A. Vinogradov and A. Leksovskii, Mater. Sci. Forum **210–213**, 549 (1996).
5. A. S. Bakaĭ, *Polycluster Amorphous Solids* (Énergoatomizdat, Moscow, 1987).
6. A. S. Bakai, in *Glassy Metals III*, Ed. by H. Beck and H.-J. Guentherodt (Springer-Verlag, Heidelberg, 1994), p. 209.
7. F. Spaepen, in *Physics of Defects*, Ed. by R. Balian, M. Kleman, and J.-P. Poirier (North-Holland, Amsterdam, 1981).
8. J. Gilman, J. Appl. Phys. **46**, 1625 (1975).
9. M. H. Cohen and G. S. Grest, Phys. Rev. Lett. **45**, 1271 (1980).
10. A. S. Argon, Phys. Chem. Solids **43** (10), 945 (1982).
11. A. M. Glezer and B. V. Molotilov, *Structure and Mechanical Properties of Amorphous Alloys* (Metallurgiya, Moscow, 1992), p. 208.
12. A. Yu. Vinogradov, K. Kitagawa, and V. A. Khonik, Fiz. Tverd. Tela (St. Petersburg) **41**, 12 (1999) [Phys. Solid State **41**, 1989 (1999)].
13. M. K. Miller, A. Cereso, M. G. Hetherington, and G. D. W. Smith, *Atom Probe Field Ion Microscopy* (Clarendon, Oxford, 1996).
14. A. S. Bakaĭ, I. M. Mikhaĭlovskiĭ, P. Ya. Poltinin, and L. I. Fedorova, Vopr. At. Nauki Tekh., No. 3 (45), 44 (1988).
15. I. M. Mikhaĭlovskiĭ, L. I. Fedorova, and P. Ya. Poltinin, Fiz. Met. Metalloved. **76**, 123 (1993).
16. S. A. Bakaĭ, I. M. Neklyudov, V. I. Savchenko, and Yu. Ékert, Vopr. At. Nauki Tekh., No. 2, 12 (2001).

*Translated by V. Sakun*

JETP Letters, Vol. 76, No. 4, 2002, pp. 222–226. Translated from Pis'ma v Zhurnal Éksperimental'noĭ i Teoreticheskoĭ Fiziki, Vol. 76, No. 4, 2002, pp. 258–262.


# Cyclotron Resonance in the InAs/GaSb Heterostructure in an Inclined Magnetic Field

**A. A. Greshnov, G. G. Zegrya*, Yu. B. Vasil'ev, S. D. Suchalkin, B. Ya. Mel'tser, S. V. Ivanov, and P. S. Kop'ev**

*Ioffe Physicotechnical Institute, Russian Academy of Sciences, Politekhnicheskaya ul. 26, St. Petersburg, 194021 Russia*
**e-mail: zegrya@theory.ioffe.rssi.ru*

Received July 11, 2002

The mechanism of cyclotron resonance line splitting in the InAs/GaSb heterostructure in an inclined magnetic field has been studied experimentally and theoretically. It is shown that the admixing of electron and hole states leads to anticrossing of the Landau levels and, hence, to splitting of the cyclotron resonance line. In the case of an inclined magnetic field, the splitting is not observed, which is explained by the suppression of the admixing of electron and hole states due to the occurrence of an additional barrier for electrons and holes given a longitudinal magnetic field component. © *2002 MAIK "Nauka/Interperiodica".*

PACS numbers: 75.70.Ak; 76.40.+b; 71.70.Di

The valence band top of GaSb in the InAs/GaSb heterostructure lies higher in energy than the conduction band bottom of InAs, which leads to the possibility of the admixing of electron and hole states [1]. Studying cyclotron resonance (CR) in such structures reveals splitting of the CR line [2]. In early publications, this effect was related to the Coulomb interaction of electrons and holes in the heterostructure [3, 4]. However, such a mechanism, acting simultaneously with the admixing of electron and hole states, makes no conspicuous contribution to the CR spectrum. In the framework of this work, the splitting of the CR line is explained by the admixing of electrons from InAs and holes from GaAs [5, 6]. This admixing, as is shown below, leads to the anticrossing of the Landau levels of electrons and holes. The optical transitions to the anticrossing level are allowed, which results in the splitting of the cyclotron absorption line. The experiments on observing CR in an inclined magnetic field point to the absence of the splitting of the cyclotron absorption line at angles of order 60°. Previously, the splitting of the CR line in an inclined magnetic field was observed in [7]; however, no explanation of this effect has been available in the literature so far.

In this work, a mechanism of suppressing the splitting of the CR line in an inclined magnetic field is proposed and investigated. The absence of the splitting is explained by suppressing the admixing of electron and hole states on increasing the longitudinal magnetic field component because of the occurrence of an additional potential barrier for electrons and holes. As a result, the magnitude of the anticrossing of the Landau levels significantly decreases, and along with it the splitting of the CR line.

**Experiment.** The samples under study were grown by the MBE technique and consisted of a single quantum well 200 Å thick separated from the GaSb layer by the AlSb barrier. The barrier thickness for various samples was 0, 6, and 20 Å. Magnetooptical measurements in the far infrared region were performed with the use of a Fourier spectrometer and a gas light-pumped laser in magnetic fields up to 23 T. Detectors of two types were used: a silicon bolometer and a GeGa photoconductive detector. The measurements were performed at a temperature of about 2 K.

Figure 1 shows two series of CR line in a transverse ($\alpha = 0°$) and inclined ($\alpha = 60°$) magnetic fields for a sample with an AlSb barrier 6 Å thick. Both spectra are shown near the values of the transverse magnetic field component $H\cos\alpha$ of order 7 T, which corresponds to the condition of strong admixing of two (electron and hole) Landau levels. The CR spectrum was approximated by two Lorentzians *CR*1 and *CR*2. In the case of the transverse magnetic field (Fig. 1a), the *CR*2 curve becomes conspicuous at fields on the order of 6.5 T. Its peak lies at higher than the peak of *CR*1, and its half-width exceeds the half-width of *CR*1 several times. As the magnetic field increases, the peak amplitude of the second curve (*CR*2) increases, whereas the intensity of the first curve (*CR*1) decreases. As the field further increases, the *CR*1 curve disappears and the CR line is approximated well by *CR*2. A plot of transition energies vs. magnetic field for *CR*1 and *CR*2 lines is displayed in Fig. 2. The transition energies related to *CR*1 depend linearly on the magnetic field with an effective mass of $0.04m_0$. The *CR*2 line also depends linearly on the magnetic field; however, it is displaced with respect to *CR*1 by 1.5 meV. As the *CR*1 line disappears, the second line becomes broader and occupies its position in energy.

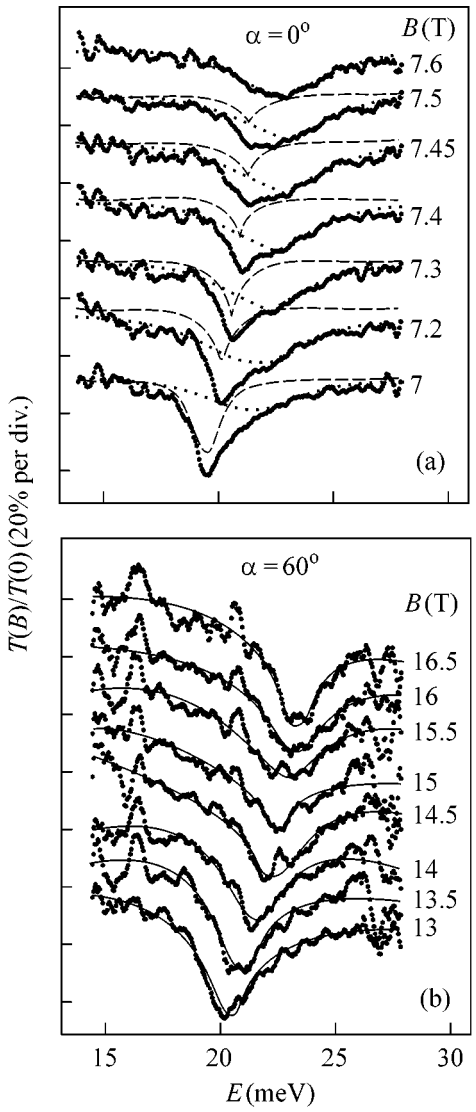


**Fig. 1.** Cyclotron resonance spectrum in an InAs/GaSb heterostructure in (a) a transverse magnetic field and (b) in an inclined magnetic field.

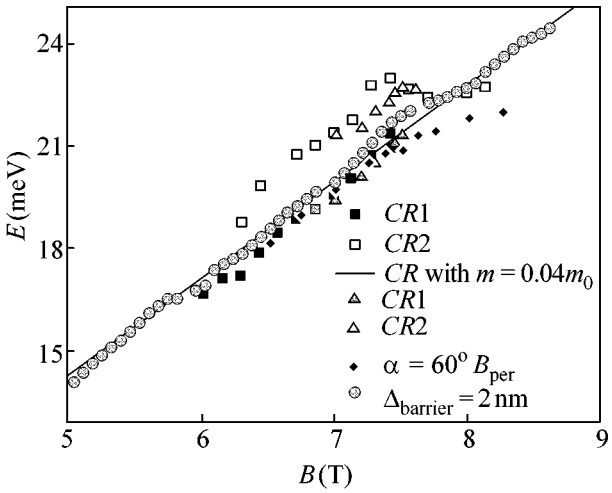


**Fig. 2.** Dependence of the optical transition energy in an InAs/GaSb heterostructure on the strength of the external magnetic field.

The splitting of the CR line is observed only in the vicinity of broadening, which confirms the admixing of electron and hole states. Similar features of the CR line were observed in a sample that contained no barrier between InAs and GaSb. In this case, the energy gap was 3.5 meV rather than 1.5 meV for a sample with an AlSb barrier 6 Å thick, which is explained by the decrease in mixing as the barrier width increases. Thus, the experiment proves the connection between the observed features of the CR line and the admixing of electron and hole states.

Additional information on the nature of mixed states was obtained on observing CR in an inclined magnetic field. The CR spectrum for the inclination angle $\alpha = 60°$ (Fig. 1b). It is clearly seen that the spectrum in this case is described well by one Lorentzian, and its position coincides with the *CR*1 line in a transverse field. In this case, the longitudinal magnetic field component eliminates only the upper line, leaving the lower one unchanged. Note that, simultaneously with the disappearance of the splitting of the CR line, strong oscillations of the amplitude and the absorption line width studied previously [8, 9] disappeared as well. This fact indicates that admixing disappears in the presence of a sufficiently strong longitudinal magnetic field component. Figure 2 also demonstrates the dependence of the absorption peak energy on the magnitude of the magnetic filed for a sample with a barrier thickness of 20 Å, which coincides with the position of the *CR*1 line. The admixing of electron and hole states in this sample is strongly suppressed, and absorption occurs on transitions between purely electronic states.

Thus, the results point to distinctions between the nature of the upper *CR*2 and lower *CR*1 CR lines. This is confirmed by the following facts. First, the *CR*2 line is always wider than *CR*1. Second, the *CR*2 peak is not symmetric with respect to the line passing through the origin of coordinates. Third, the longitudinal magnetic field component differently affects the *CR*1 and *CR*2 line, so that only *CR*2 becomes suppressed. Thus, the results demonstrate that in a narrow range of fields, a *CR*2 line shifted in energy is added to the purely electronic *CR*1 line. The half-width of the former line exceeds the half-width of *CR*1 several times. The given line should be assigned to transitions between purely electronic and mixed states.

**Theory.** In order to analyze the experimental results, it is necessary to determine the spectrum and wave functions of carriers in the InAs/GaSb heterostructure. To describe the spectrum accurately, we will use the four-band Kane model. Within this model, the

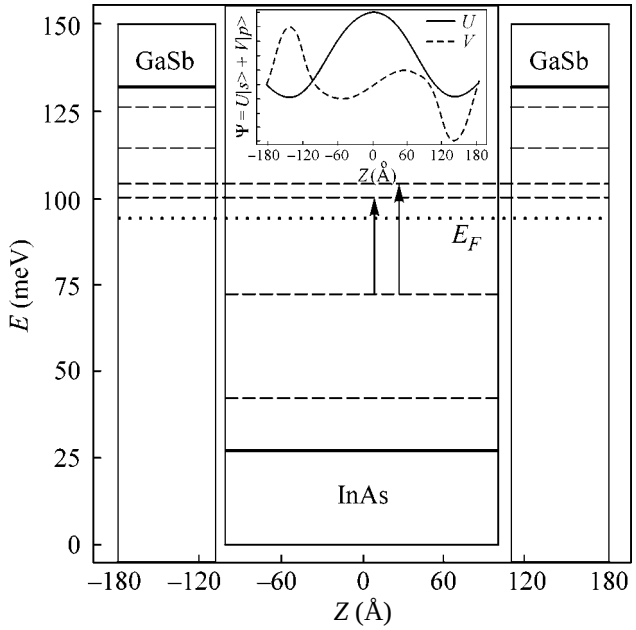


**Fig. 3.** Approximation of the potentials and the scheme of energy levels of electrons and holes in an InAs/GaSb heterostructure. Arrows indicate the allowed optical transitions between the Landau levels. The inset presents schematically wave functions of mixed states.

wave functions of carriers represent a superposition of *s*-type electronic states and *p*-type hole states

$$\psi = U|s\rangle + \mathbf{V}|\mathbf{p}\rangle,$$

where $|s\rangle$ and $|\mathbf{p}\rangle$ are Bloch functions with angular momenta of 0 and 1, respectively; and $U(\mathbf{r})$ and $\mathbf{V}(\mathbf{r})$ are smooth envelopes of the spinor Bloch functions. In the presence of an external magnetic field, the system of equations for envelopes in the vicinity of the Γ point takes the form [10]

$$\begin{aligned}(E_c - \boldsymbol{\mu}\mathbf{H} - E)U + \gamma\hat{\mathbf{K}}\mathbf{V} &= 0,\\ \gamma\hat{\mathbf{K}}U + \left(E_v - \delta - \boldsymbol{\mu}\mathbf{H} - \frac{\hbar^2\hat{\mathbf{K}}^2}{2m_h} - E\right)\mathbf{V} + i\delta[\boldsymbol{\sigma}\times\mathbf{V}] &= 0.\end{aligned} \quad (1)$$

Here, γ is the Kane matrix element, $m_h$ is the mass of heavy holes, $\delta = \Delta_{so}/3$, $\Delta_{so}$ is the spin–orbit coupling constant, $E_c$ and $E_v$ are the energies of the conduction band bottom and the valence band top, $\boldsymbol{\sigma} = (\sigma_x, \sigma_y, \sigma_z)$ are the Pauli matrices, $\boldsymbol{\mu} = -(g_0/2)\mu_B\boldsymbol{\sigma}$ is the magnetic moment of an electron, $\mu_B$ is the Bohr magneton, $g_0$ is the *g*-factor of a free electron, $\hat{\mathbf{K}} = -i\nabla - (e/c\hbar)\mathbf{A}$ is the generalized wave vector of a particle, and $\mathbf{A}$ is the vector potential of the field.

The system of equations (1) consistently takes into account the spin–orbit interaction, which essentially affects the spectrum of carriers in a magnetic field. When solving the Kane equations for the InAs/GaSb heterostructure, we approximated the quantum wells for electrons and holes by a rectangular potential. The *z* axis is directed perpendicular to the heteroboundaries; the quantum well for electrons is located in the region $|z| < a$, and the quantum well for holes, in the region $a < |z| < b$. The geometry of the system described above and the qualitative pattern of energy levels for the case of a transverse magnetic field are displayed in Fig. 3.

In the case when the magnetic field is directed at an arbitrary angle to the heteroboundary plane, it is convenient to orient the *x* axis perpendicular to *H*. Let us select the vector potential in the following form:

$$\mathbf{A} = (Hz\sin\alpha - Hy\cos\alpha, 0, 0), \quad (2)$$

where α is the angle between the direction of the magnetic field and the *z* axis, and $\mathbf{H} = H(0, \sin\alpha, \cos\alpha)$. This allows one to separate the variables and to reduce the problem to a two-dimensional one. In this gauge, the quantum number $k_x$ is conserved. The complete separation of variables is possible in the cases of transverse ($\alpha = 0$) and longitudinal ($\alpha = \pi/2$) directions of the magnetic field *H*.

For a transverse magnetic field, the vector potential, according to Eq. (2), depends only on the *y* coordinate: $\mathbf{A} = (-yH, 0, 0)$ (Landau gauge). The solution of the Kane equations (1) is a superposition of $l\uparrow$ and $((l+1)\downarrow$ states corresponding to different spin directions. Here, the quantum number *l* is a sum of the angular momentum and the Landau level number. In particular, for the purely electronic states of the $|s\rangle$-type, *l* coincides with the magnetic quantization level number.

In the approximation taken here for the heterostructure potential, the quantum wells for holes are located symmetrically with respect to the quantum well for electrons. In this case, the wave functions for electrons are separated by parity, depending on the spin direction. The boundary conditions at $z = 0$ for solutions differing in parity have the following form:

$$\begin{aligned}U\uparrow = V_x\uparrow = V_y\uparrow = V_z\downarrow &= 0,\\ \frac{d}{dz}U\downarrow = \frac{d}{dz}V_x\downarrow = \frac{d}{dz}V_y\downarrow = \frac{d}{dz}V_z\uparrow &= 0,\end{aligned} \quad (3)$$

$$\begin{aligned}U\downarrow = V_x\downarrow = V_y\downarrow = V_z\uparrow &= 0,\\ \frac{d}{dz}U\uparrow = \frac{d}{dz}V_x\uparrow = \frac{d}{dz}V_y\uparrow = \frac{d}{dz}V_z\downarrow &= 0.\end{aligned} \quad (4)$$

At $|z| = b$ points, the boundary conditions are reduced to the vanishing of the $V_x$, $V_y$, and $V_z$ components of the wave function. The hole states have no symmetry, which leads to significant mixing of the $l\uparrow$ and $((l+1)\downarrow$ states.

In the absence of electron–hole admixing, an approximate spectrum of carriers can bee obtained analytically. In this case, the spectrum is weakly nonparabolic, which is favored by the monotonic decrease in the *g*-factor with the magnetic field. The sign of the *g*-factor remains unchanged with increasing field.

The spectrum of carriers calculated with taking into account the admixing of electron and hole states differs from that described above, and qualitative effects (anticrossings) arise in the vicinity of the points of intersection of various nonperturbed curves $E(H)$. Note that the magnitude of anticrossing (the energy gap between the electron and hole bands) depends on the behavior of curves $E(H)$ corresponding to electron and hole states and also on their spin composition. The behavior of curves is determined by their inclination ($g$-factor) and depends on the magnitude of the magnetic field. The variation of the $g$-factor with increasing field is essential for the heavy hole states because of admixing of the light and heavy hole states [10].

A portion of the plot of the energy of states vs. magnetic field is given in Fig. 4 for the following values of quantum numbers: $l = 3$, $s = \pm 1/2$. Curves with $s = -1/2$ are shown in solid lines, and those with $s = +1/2$, in dashed lines. The curves going down in energy correspond to two branches of heavy holes, which are degenerate at $H = 0$. In this case, both electronic and hole curves correspond to the ground size-quantization state of. It is evident in Fig. 4 that the anticrossing of the Landau levels of electrons and holes occurs at a certain value of the magnetic field. This means that strong admixing of electron and hole states exists at this value of the magnetic field. The magnitude of anticrossing (energy gap) for each pair of electronic and hole curves is in agreement with experimental data, and the accurate value is determined by the quantitative relationship between the $|s\rangle$ and $|\mathbf{p}\rangle$ wave-function components of the electron and hole states corresponding to anticrossing curves. The range of magnetic fields $\Delta H \approx 0.5$ T in which the curve $E(H)$ transforms from the electronic to hole type is also in agreement with experiment. The precise width of this range is also determined by the specific relationship between the wave-function components. The shape of wave functions near the anticrossing is qualitatively depicted in the inset in Fig. 3. Here, by $s$ and $p$ we mean the sets of the corresponding two and six wave-function components. On passing through the anticrossing region, the wave function steadily transforms from the electronic to hole type. Similar calculations for a transverse magnetic field in a somewhat different model were performed in [11].

The results observed in CR experiments are associated with optical transitions between various energy states. To accurately determine the transitions that occur experimentally, it is necessary to know accurately the potential and the Fermi level in the heterostructure under consideration. However, even within the frameworks of the model in hand, one may infer that the observed effects are associated with the coexistence of transitions between an electron (or hole) state and two close mixed states. The shape of the CR line in this case is a superposition of two Lorentzians $I(E) = CR1 + CR2$ and is transformed from $CR1$ to $CR2$ within a certain range of fields. Quantitative calculations demonstrated

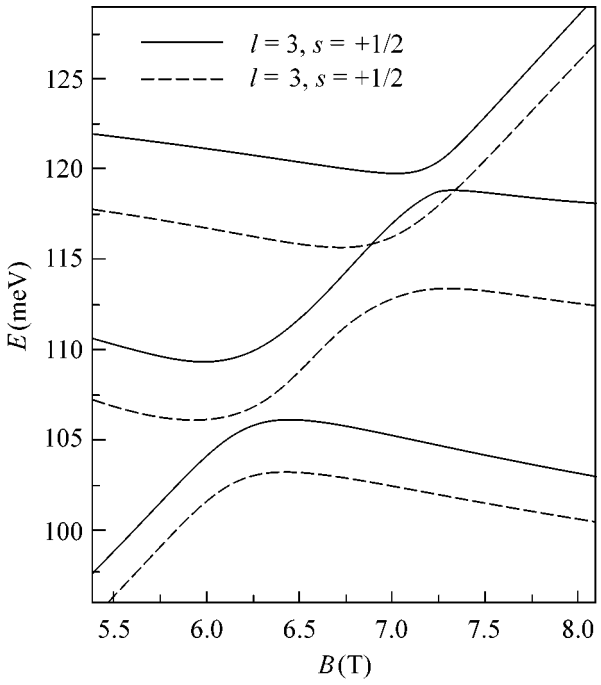


**Fig. 4.** Dependence of the energy of mixed states on the strength of a transverse external magnetic field.

a good agreement between the anticrossing magnitude and the experimental data (3–4 meV).

To analyze the suppressing of the effects associated with electron–hole admixing in an inclined magnetic field, consider the limiting case of a longitudinal field direction ($\alpha = \pi/2$). The vector potential, according to Eq. (2), depends only on the $z$ coordinate, $\mathbf{A} = (zH, 0, 0)$. The energy of the states under consideration in a longitudinal field is summed up of two parts connected with size and magnetic quantization. These energies can be separated analytically only in the cases $k_z/k_H \gg 1$ or $k_H/k_z \gg 1$ (weak and strong magnetic fields). In our problem, an intermediate case is of interest. The boundary conditions in the case of a longitudinal magnetic field require the continuity of the same quantities as in the transverse case. However, the boundary conditions at $z = 0$ differ from the case of a transverse field. The wave functions are also even or odd functions of the coordinates; however, the parity of the state corresponds to even and odd size-quantization levels rather than different spin directions.

The effective potential for electron and hole quantum wells in a longitudinal magnetic field is summed up from the rectangular component and an additional potential associated with the presence of an external field. In the parabolic approximation, the effective values $E_c$ and $E_v$ have the following coordinate dependence:

$$E_c(z) = E_c + \frac{\hbar^2 k_H^2}{2m_c}(z - z_0)^2 \sin^2\alpha,$$

$$E_v(z) = E_v - \frac{\hbar^2 k_H^2}{2m^*}(z - z_0)^2 \sin^2\alpha,$$

where $m^* = (m_h, m_l)$ are, respectively, effective masses for the heavy and light holes; $z_0$ are the centers of the electron and hole wells. The appearance of an additional potential in the form of an addition to $E_c$ and $E_v$ quadratic in $z$ leads to a decrease in admixing of electrons and holes, because the barrier height increases much faster than the increase in the energy of states with increasing longitudinal magnetic field.

Thus, in the case of large inclination angles at which the longitudinal field component cannot be neglected, the effects associated with electron–hole admixing decrease significantly. This fact is explained by the occurrence of an additional parabolic barrier for electrons and holes due to the longitudinal magnetic field component, which hinders the admixing of carriers. In this case, the magnitude of anticrossing must monotonically decrease with increasing $\alpha$. In particular, calculations showed a decrease in the magnitude of anticrossing by two orders of magnitude in passing from the transverse to longitudinal direction of the field. Experimentally, these effects disappear at angles $\alpha$ of order 60°.

This work was supported by INTAS (project no. 99-01146) and the Russian Foundation for Basic Research (project nos. 01-07-90299, 01-07-90300, and 02-02-17610).

## REFERENCES

1. M. Altarelli, Phys. Rev. B **28**, 842 (1983).
2. D. Heitmann, M. Ziesmann, and L. L. Chang, Phys. Rev. B **34**, 7463 (1986).
3. J. Cono, B. D. McCombe, and J.-P. Cheng, Phys. Rev. B **50**, 12242 (1994).
4. R. J. Warburton, B. Brar, C. Gauer, *et al.*, Solid-State Electron. **40**, 679 (1996).
5. M. J. Yang, C. H. Yang, B. R. Bennett, and B. V. Shanabrook, Phys. Rev. Lett. **78**, 4613 (1997).
6. M. Lakrimi, S. Khym, R. J. Nicholas, *et al.*, Phys. Rev. Lett. **79**, 3034 (1997).
7. T. P. Marlow, L. J. Cooper, D. D. Arnone, *et al.*, Phys. Rev. Lett. **82**, 2362 (1999).
8. S. D. Suchalkin, Yu. B. Vasil'ev, K. von Klitzing, *et al.*, Pis'ma Zh. Éksp. Teor. Fiz. **68**, 753 (1998) [JETP Lett. **68**, 792 (1998)].
9. Yu. Vasilyev, S. Suchalkin, K. von Klitzing, *et al.*, Phys. Rev. B **60**, 10636 (1999).
10. G. G. Samsonidze and G. G. Zegrya, Phys. Rev. B **63**, 075317 (2001).
11. S. F. Tsay, J. C. Chiang, Z. M. Chau, and I. Lo, Phys. Rev. B **56**, 13242 (1997).

*Translated by A. Bagatur'yants*

JETP Letters, Vol. 76, No. 4, 2002, pp. 227–230. Translated from Pis'ma v Zhurnal Éksperimental'noĭ i Teoreticheskoĭ Fiziki, Vol. 76, No. 4, 2002, pp. 263–266.


# Inverse Crystallization of a System of Abrikosov Vortices with Periodic Pinning

**M. V. Zyubin, I. A. Rudnev, and V. A. Kashurnikov***

*Moscow Institute of Engineering Physics, Kashirskoe sh. 31, Moscow, 115409 Russia*

** e-mail: kash@cityline.ru*

Received July 2, 2002; in final form, July 17, 2002

A system of vortices in a quasi-two-dimensional HTSC plate with periodic pinning is considered. The magnetization curves are calculated by the Monte Carlo method for different values of an external magnetic field and different temperatures. It is shown that the vortex system with periodic pinning may crystallize with an increase in temperature. © *2002 MAIK "Nauka/Interperiodica".*

PACS numbers: 74.60.Ge; 74.76.Bz; 74.80.Dm

The physics of the vortical state demonstrate a high diversity of phase transformations [1]. The nature of various phase states of vortex systems and the transitions between them have been the subject of extensive studies, both theoretical and experimental. It was established that, at low temperatures, the vortex system forms a triangular lattice. The temperature fluctuations can destroy the vortex crystal in HTSC and induce transition to the vortex liquid phase. Defects and impurities have a sizable effect on the HTSC phase diagram. The defects can often lead to new phase states of the vortex system. It was shown in [2, 3] that the introduction of even a small amount of defects gives rise to a new phase with orientational melting of vortex lattice.

Recently, considerable progress has been achieved in the methods of creating artificial defects (see, e.g., [4]). Modern techniques allow the creation of pinning centers with the predetermined parameters. The artificial creation of pinning centers allows the study of the influence of defects on the HTSC phase diagram with fully controlled parameters of defect structure. Recently, special interest has been shown in the problem of periodic pinning. The presence of a pinning center lattice gives rise to the effects associated with the correspondence between the number of vortices and defects. These effects cause the formation of ordered configurations in the vortex system, which are substantially different from the familiar triangular lattice [5]. In turn, experiments show that the ordering in the vortex system gives rise to the singularities in the magnetization curves $M(H)$ and in the magnetic-field dependences of critical current and electrical resistance [4, 5].

In this work, we present new results of Monte Carlo modeling the vortex system with periodic pinning. It is shown that the magnetization curves have singularities that are caused by the influence of the periodic lattice of pinning centers. The vortex distribution patterns are obtained for different points on the $M(H)$ curve.

We have found that the vortex system with periodic pinning becomes ordered with an increase in temperature (inverse crystallization effect). Such an unusual behavior rarely occurs in nature. The inverse crystallization was observed in some magnetic materials [6] and polymer systems [7]. Recently [8], the inverse crystallization of a vortex system was observed in the case of chaotic pinning. The nature of inverse crystallization in the presence of periodic pinning, which is predicted in this work, is basically different from the chaotic case.

We consider a three-dimensional bulk HTSC sample having layered structure in the *xy* plane. The sample has a finite thickness in the *x* direction and is infinite in the *y* and *z* directions. It is placed in a magnetic field aligned with the *z* axis to eliminate the demagnetization effects. We assume that the interlayer interaction in HTSC is weak and consider only a quasi-two-dimensional *xy* plate with thickness *d* to model a superconducting layer; i.e., we "cut out" a layer with thickness *d* along the *z* axis and consider it in our calculations. The sample boundaries in the *x* direction are the vortex sources, and the Meissner currents flow at a penetration depth. The thermodynamic Gibbs potential of the vortex system in the plate has the form

$$G = \frac{1}{2}\sum_{i \neq j} U(r_{ij}) + \sum_i U_p(r_i) + \sum_i U_m(r_i) + U_{\text{self}} + U_{\text{surf}}. \quad (1)$$

It includes the energies $U(r_{ij})$ of pair interaction between vortices, the energies $U_p(r_i)$ of interaction between vortices and pinning centers, the energies $U_m(r_i)$ of interaction between vortices and Meissner currents, the self-energy $U_{\text{self}}$ of the vortex system, and

0021-3640/02/7604-0227$22.00 

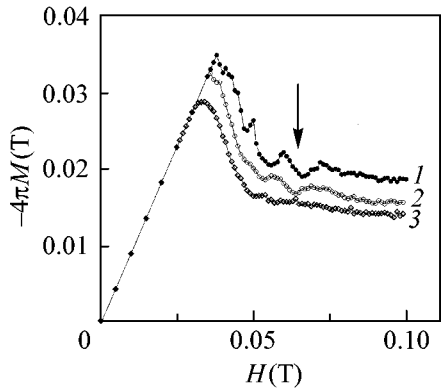


**Fig. 1.** Magnetization curves for a triangular lattice of pointlike pinning centers with concentration $n_d$ = 5.7 μm$^{-2}$ at different temperatures: $T$ = (*1*) 1, (*2*) 5, and (*3*) 10 K. Arrow indicates the magnetic field corresponding to the inverse crystallization of the vortex system.

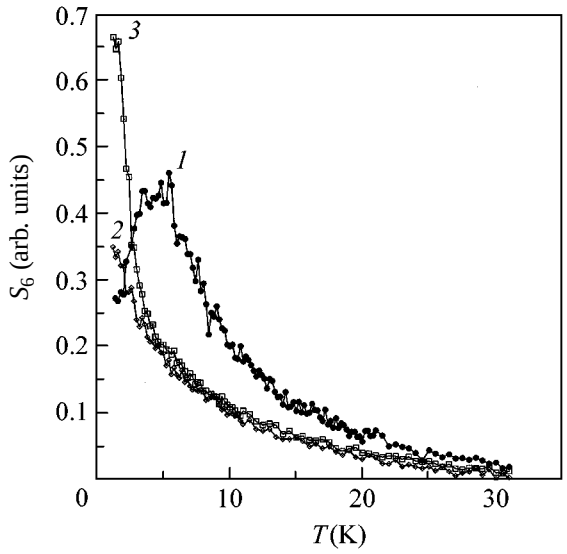


**Fig. 2.** Temperature dependence of the structure factor $S_6$ for the (*1*) triangular defect lattice with $n_d$ = 5.7 μm$^{-2}$, (*2*) chaotic defect arrangement with $n_d$ = 5.7 μm$^{-2}$, and (*3*) pure superconductor.

the interaction $U_{\text{surf}}$ of the vortex system with the superconductor surface (see model in [9]).

The calculations were carried out by the method based on the Monte Carlo algorithm for grand canonical ensemble. This method allows one to determine the equilibrium distribution of vortex density for fixed external parameters (magnetic field $H$, temperature $T$, distribution of pinning centers, and their type) and calculate the magnetization $M$ and magnetic flux density $B$ for the resulting distribution. Therefore, the method can be used for obtaining both the integral superconductor characteristics and the visual magnetic-flux distribution pattern. This approach has a number of fundamental distinctions as compared to the conventional calculations, namely, the highly precise accounting of the influence of plate boundaries, wide temperature range $0 < T < T_c$, and the possibility of considering any distribution for defects of any type. The method of calculation and the model were described in detail in [9, 10].

The modeling was carried out using the parameters of a layered $Bi_2Sr_2CaCu_2O_8$ superconductor: $d$ = 0.27 nm, $\lambda_0$ = 180 nm, $\xi_0$ = 2 nm, and $T_c$ = 84 K [11]. The pinning depth was taken to be sufficiently large to exclude the temperature depinning. The calculations were performed for plates with size 5 × 2.25 μm over the range of external fields $0 \le H \le 0.1$ T. The maximal range of external field $H$ was limited only by the computer power and, hence, by the CPU time.

We calculated the magnetic-field dependences of magnetization for various temperatures and the triangular lattice of pointlike pinning centers with concentration $n_d$ = 5.7 μm$^{-2}$. One can see from Fig. 1 that the curves show a number of clearly-defined features at low temperatures $T$ = 1 and 5 K. These features are due to the correspondence effect between the numbers of vortices and defects. At certain ratios between the number $N_v$ of vortices and the number $N_d$ of defects, ordered configurations appear in the vortex system. For example, the triangular vortex lattice shown in Fig. 3b corresponds to the case where the number of vortices is four times larger than the number of defects, $N_v/N_d$ = 4. It should be noted that the vortex lattice is not formed at an arbitrary integer value of the $N_v/N_d$ ratio. It was demonstrated in [12] by the molecular dynamic study that the ordered configurations for the triangular lattice of pinning centers appear at the following ratios between the numbers of vortices and defects: $N_v/N_d$ = 1, 2, 3, 4, 7, 9, 12, 13, 16, 19, 21, 25, and 28. In this work, the features in the magnetization curves were observed at $N_v/N_d$ = 2, 3, and 4. The higher order features lie beyond the range of magnetic fields used in our calculations.

As the external magnetic field increases, the "rigid" vortex lattice prevents the penetration of new vortices into the sample, and the magnetization increases. On further rise in magnetic field, additional vortices can enter the sample to destroy the ordered vortex structure and reduce the magnetization. To proceed, it should be emphasized that the ordered configurations are observed not at the point corresponding to the local magnetization maximum but at the base of the ascending portion of magnetization curve.

With an increase in temperature, the Meissner superheating field decreases and the magnetization curves run lower. The peaks shift to lower fields, and their magnitudes decrease. On further rise in temperature, the features fully disappear. An analysis of the vor-

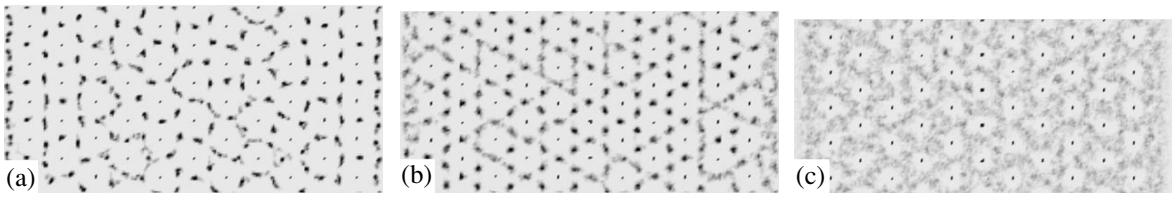


**Fig. 3.** Vortex density distribution in the field $H = 0.062$ T at different temperatures for the triangular defect lattice with $n_d = 5.7\ \mu m^{-2}$; $T$ = (a) 1, (b) 5.2, and (c) 30 K.

tex density distributions indicates that the peaks disappear because of the melting of the vortex lattice.

Inasmuch as the peak positions undergo shift with changing temperature, a situation is possible where the descending portion at low temperature corresponds to the peak base at a higher temperature (e.g., the descending portion following peak *2* at $T = 1$ K and the peak base at $T = 5$ K in Fig. 1). Thus, the transition from the disordered to ordered configuration may occur with an increase in temperature. The peak widths in the magnetization curve strongly depend on the potential well depth of defects. Note that the ascending portion after the minimum goes almost at an angle of 45°, indicating a nearly "Meissner-type" behavior, and the breaking point corresponds to the "break" of the first vortex through the blockade produced by the fields of vortices that are already pinned and form regular lattice. The larger the pinning strength, the larger the breaking field (an analog of the Meissner superheating field). For this reason, one can provide favorable conditions for the effect by choosing the appropriate range of the defect depths.

To verify this assumption, we calculated the configuration of vortex system at a fixed field $H = 0.062$ T and various temperatures. The following situations were considered: a triangular lattice of point defects with $n_d = 5.7\ \mu m^{-2}$; the chaotic distribution of point defects with $n_d = 5.7\ \mu m^{-2}$; and a pure sample. To characterize the degree of ordering in the system, the structure factor $S_6$ was calculated,

$$S_6 = \sum_{i=1}^{N_v} \frac{1}{Z_i} \sum_{j=1}^{Z_j} e^{i6\theta_{ij}}. \qquad (2)$$

Here, $Z_i$ is the coordination number of the $i$th vortex and $\theta_{ij}$ is the angle between the nearest neighbors. The temperature dependences of $S_6$ are shown in Fig. 2. In the case of periodic arrangement of pinning centers, $S_6$ increases at temperatures $T = 1$–5.8 K; i.e., the vortex system becomes more ordered with an increase in temperature. At $T = 1$ K (Fig. 3a), the vortex system becomes disordered, in spite of the low temperature, because the number of vortices is not a multiple of the number of defects. As the temperature incenses, new vortices enter the sample, and a new commensurable stable ordered configuration arises (Fig. 3b), which again melts upon further rise in temperature (Fig. 3c). Thus, in the case of periodic arrangement of defects, the vortex system can crystallize upon an *increase* in temperature. This is accompanied by the appearance of singularities in the derivative of magnetization with respect to temperature; the recrystallization points can be derived from these singularities. For the chaotic defect distribution and in a pure sample, the structural parameters gradually decrease with increasing temperature over the entire temperature interval studied (Fig. 2).

It should be noted that the inverse crystallization was experimentally observed in [8] in a system with chaotic pinning. In the case of chaotic defect arrangement, the vortex system becomes ordered, because the pinning weakens with increasing temperature, while the interaction of vortices leads to a triangular lattice. As was mentioned above, we assume that the pinning centers are sufficiently deep for the temperature-induced depinning to be excluded. For this reason, the inverse crystallization in our case has a basically different physical nature. The system becomes ordered with a rise in temperature due to the correspondence between the numbers of vortices and defects.

In summary, we have reported the results of Monte Carlo modeling the vortex system with periodic pinning. It has been shown that the periodic arrangement of defects gives rise to the singularities of various nature in the magnetization curves. The temperature behavior of the system with periodic pinning has been analyzed. It has been shown that, in this case, the vortex system can undergo ordering upon an increase in temperature, as a result of the penetration of new vortices and formation of the stable configuration.

The inverse crystallization of vortex system can be visualized in superconductors with periodic arrangement of artificial pinning centers using the magneto-optical techniques or high-resolution scanning magnetometry.

This work was supported by the Russian Foundation for Basic Research (project no. 00-02-17803), the Federal Program "Integratsiya" (project no. B-0048), and the Subprogram "Superconductivity" of the State Scientific and Technical Program "Topical Directions in Condensed State Physics."

## REFERENCES


1. E. H. Brandt, Rev. Prog. Phys. **58**, 1465 (1995).
2. M. E. Gracheva, V. A. Kashurnikov, and I. A. Rudnev, Pis'ma Zh. Éksp. Teor. Fiz. **66**, 269 (1997) [JETP Lett. **66**, 291 (1997)].
3. V. A. Kashurnikov, I. A. Rudnev, M. E. Gracheva, and O. A. Nikitenko, Zh. Éksp. Teor. Fiz. **117**, 196 (2000) [JETP **90**, 173 (2000)]; I. A. Rudnev, V. A. Kashurnikov, M. E. Gracheva, *et al.*, Physica C (Amsterdam) **332**, 383 (2000).
4. D. J. Morgan and J. B. Ketterson, J. Low Temp. Phys. **122**, 37 (2001).
5. A. N. Grigorenko, G. D. Howells, S. J. Bending, *et al.*, Phys. Rev. B **63**, 052504 (2001).
6. Y. Yeshurun, M. B. Salamon, K. V. Rao, *et al.*, Phys. Rev. Lett. **45**, 1366 (1980).
7. A. L. Greer, Nature **404**, 34 (2000).
8. N. Avraham, B. Khaykovich, Y. Myasoedov, *et al.*, Nature **411**, 451 (2001).
9. V. A. Kashurnikov, I. A. Rudnev, and M. V. Zyubin, Zh. Éksp. Teor. Fiz. **121**, 442 (2002) [JETP **94**, 377 (2002)].
10. V. A. Kashurnikov, I. A. Rudnev, and M. V. Zubin, Supercond. Sci. Technol. **14**, 695 (2001).
11. S. L. Lee, P. Zimmermann, H. Keller, *et al.*, Phys. Rev. Lett. **71**, 3862 (1993).
12. S. Reichhardt, C. J. Olson, and Franco Nori, Phys. Rev. B **57**, 7937 (1998).


*Translated by V. Sakun*

JETP Letters, Vol. 76, No. 4, 2002, p. 231.

**ERRATA**

# Erratum: Nonsinusoidal Current–Phase Relation in SFS Josephson Junctions (Pis'ma Zh. Éksp. Teor. Fiz. 75, 709 (2002) [JETP Lett. 75, 558 (2002)])

**A. A. Golubov[1], M. Yu. Kupriyanov[2], and Ya. V. Fominov[3, 1]**

[1] *Department of Applied Physics, University of Twente, 7500 AE Enschede, The Netherlands*
*e-mail: a.golubov@tn.utwente.nl*
[2] *Nuclear Physics Institute, Moscow State University, Vorob'evy Gory, Moscow, 119899 Russia*
*e-mail: mkupr@pn.sinp.msu.ru*
[3] *Landau Institute for Theoretical Physics, Russian Academy of Sciences, ul. Kosygina 2, Moscow, 117940 Russia*
*e-mail: fominov@landau.ac.ru*

PACS numbers: 75.50.+r; 74.80.-g; 99.10.+g

In reproducing Fig. 5 from the article A.A. Golubov, M.Yu. Kupriyanov, and Ya.V. Fominov (Pis'ma Zh. Éksp. Teor. Fiz. **75**, 709 (2002) [JETP Lett. **75**, 558 (2002)]), the figure was corrupted. Its correct version is given below. The editorial board and the authors present their apologies.

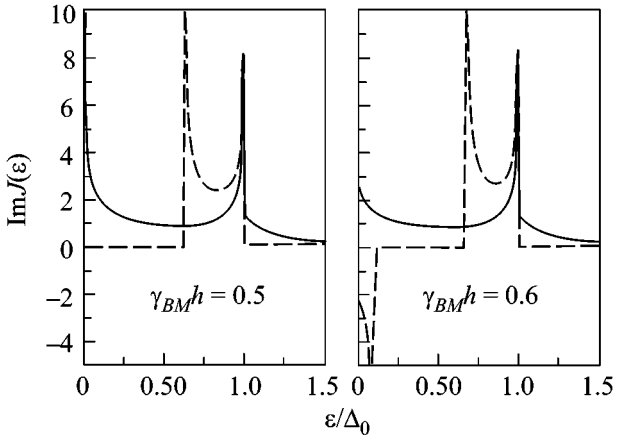

*JETP Letters, Vol. 76, No. 4, 2002, p. 231.*

**ERRATA**

# Erratum: Excitations in a Quantum Hall Ferromagnet with Strong Coulomb Interaction (Pis'ma Zh. Éksp. Teor. Fiz. 75, 419 (2002) [JETP Lett. 75, 348 (2002)])

**S. V. Iordanski and A. Kashuba**

*Landau Institute for Theoretical Physics, Russian Academy of Sciences, Moscow, 117334 Russia*

PACS numbers: 71.27.+a; 73.43.Cd; 71.35.Lk; 99.10.+g

The last paragraph in the article S.V. Iordanski and A. Kashuba (Pis'ma Zh. Éksp. Teor. Fiz. **75**, 419 (2002) [JETP Lett. **75**, 348 (2002)]) should read as follows: "This work was supported by the Russian Foundation for Basic Research (project no. 01-02-17520a), INTAS (project no. 99-01146), and by the Condensed Matter Program of the RF Ministry of Technology and Science.

The authors express their gratitude to V.T. Dolgopolov for numerous discussions."

0021-3640/02/7604-0231$22.00 